Built2Spec

Built to Specifications – Tools for the 21st Century Construction Site

H2020 Grant Agreement – 637221

D2.2 Building modelling and 3D automated referencing

Primary Author: ECN

Contributors: CEREMA - IFSTTAR - UB

1st Quality reviewer: Patrice Mestayer

2nd Quality reviewer: Pablo Speciale

Deliverable nature:	Report (R)
Dissemination level: (Confidentiality)	Public (PU)
Contractual delivery date:	**M29** – may 31st, 2017
Actual delivery date:	31 May 2017
Version:	1
Total number of pages:	69
Keywords:	Building thermal modelling, IR image registration

Table of Contents

Abbreviations

B2S = Built to Specifications

DOA = Description of Action

CS = Communication Strategy

WP = Work Package

IR = Infra-Red

CFD = Computational Fluid Dynamic

TIR = Thermal Infra-Red

Cerema = Centre d'études et d'expertise sur les risques, l'environnement, la mobilité et l'aménagement

UB = University of Bordeaux

LMA = Levenberg-Marquadt Algorithm

ECN = Ecole Centrale de Nantes

RGB = Red Green Blue, the classical type of image taken by a camera

Nomenclature

A	Absorbance	-
a	Diffusivity	$m^2 \cdot s^{-1}$
b	Effusivity	$J \cdot K^{-1} \cdot m^{-2} \cdot s^{-1/2}$
c	Specific heat capacity	$J \cdot K^{-1} \cdot kg^{-1}$
E	Energy	$W \cdot m^{-2}$
h	Heat transfer coefficient	$W \cdot K^{-1} \cdot m^{-2}$
I	Signal intensity	mW
k	Absorption coefficient	-
L	Thickness	m
q	Heat flux	$W \cdot m^{-2}$
Q	Heat flow	W
R	Thermal resistance	$K \cdot m^2 \cdot W^{-1}$
S	Area	m^2
T	Temperature	K
U	Thermal transmittance	$W \cdot K^{-1} \cdot m^{-2}$
v	wind velocity	$m \cdot s^{-1}$
V	volume	m³
k	conductance	W/K
Tri	triangle	
sky	sky	
sc	Triangle of the urban scene	
F	shape factor	
I	Loss due to infiltration	W
Q	Heating load	W
w	wall	

Greek alphabet

λ	conductivity	$W.m^{-1}.K^{-1}$
ε	Emissivity	-
θ	Temperature (Laplace transform)	K
φ	Heat flux (Laplace transform)	$W.m^{-2}$
ρ	Density	$kg.m^{-3}$
σ	Stefan-Boltzmann constant	$W.K^{-4}.m^{-2}$
τ	Solar transmission	-
α	Absorptivity	-

Subscript

air	air
t	output
0	input
r	radiant
s	surface
flu	fluid
i	indoor
o	outdoor
h	heating
c	cooling
m	maximum
conv	convection
cond	conduction
rad	radiative
LW	long wave
SW	short wave

1 Introduction

The Built2Spec project focuses on new self-inspection techniques and quality check measures. The WP2 aims at developing an integrated solution for non-intrusive evaluation of the local thermal performance values of a wall (U-values, thermal storage capacity) from external remote sensing measurements, combining TIR measurements (from already existing technology) to new quantitative analysis methods. This kind of development is still used only in the research lab.

According to the planned deliverable in the framework of the project Built2Spec, this document will be split in two parts: a first one dedicated to Building Modelling and a second one dedicated to 3D referencing.

The first part will focus on the methodology of modelling at three scales: wall, building and district. First, at the wall scale, two methods of modelling are presented: the quadrupole modelling and the finite difference modelling. These models are used both for direct and inverse approaches. Then, at the building scale, we present a detailed thermal model which integrates envelope defects. Finally, the latter is integrated to detailed external environmental conditions to assess the impact of both defects and local climate on the building energy efficiency.

The second part focus on the usable methods to align a set of 2D thermal images from a building (or buildings) onto a 3D model (or models) of the same building in order to visualize its thermal quality. First it focuses on the method used to calculate a camera pose (i.e. 3D position and 3D orientation of a camera) with respect to a 3D model. Then, it gives an overview on texture and geometric based localisation techniques. A last part will explore methods to register images and especially IR images onto visible images and how to register images with a known 3D model.

2   Building Modelling

2.1   Introduction

The work accomplished by University of Bordeaux (UB) and Cerema groups in B2S framework consists in two parts: experimental tests and numerical simulations. The experimental tests are described in deliverables D.2.3 and D.7.2. The numerical works are discussed in this deliverable.

In this section, we present methods for identifying the thermo-radiative and thermal characteristics of buildings. In thermal studies, some methods do not need both parts (experimental and numerical). They just need experimental tests to perform a quick calculation of the thermal properties of materials. This is the case of several standard methods like the Guarded Hot Plate (EN 12667, EN 12664 and EN 674) for thermal conductivity determination. UB group and Cerema group developed methods for thermo-physical properties estimation. For these methods, not only experimental tests are needed but also a numerical model. The latter, in the methods presented here, is based first on the direct heat transfer model and then on the inverse model. Thus, in the section 2.2, three numerical modelling are introduced: quadrupole model, finite difference model and Solene-Microclimat detailed modelling. The quadrupole model and finite difference model are two widely used numerical modelling in the heat transfer regime at wall scale. The aim of the work in Built2Spec project is to choose the best adapted method for different conditions. The Solene-Microlimat modelling is used for the estimation of a whole building energy efficiency. The aim is to be able to take into account the actual thermal characteristics of building elements (such as envelope with defects) and also the local environment conditions to assess the actual performance of building. In the section 2.3, two inverse models based on both quadrupole model and finite difference model are presented. These numerical models are combined to experimental tests in order to determine the thermal characteristics of the wall. The aim here is to study the feasibility of the two methods in lab conditions and to conclude on the possibility of their use on site with realistic conditions.

2.2   Direct Modelling

2.2.1   Aim

In this section, the numerical models for direct heat transfer problem based on three methods are presented and discussed.

2.2.2   Wall modelling: Quadrupole model

The thermal quadrupoles method has been introduced in detail in the book (Denis Maillet 2000). The quadrupole method is developed as a tool for new technologies of thermal property measurement. An experiment involving heat transfer is carried on the sample, whose thermal properties are unknown and to be estimated (thermal conductivity, thermal diffusivity, etc.). The thermal excitation and measured data (heat flux and temperature) are recorded. The thermal parameters of this sample can be estimated by comparing these measured data with the output of a thermal model (for example, through least squares minimization). When applying the quadrupole method to the heat equation, the thermal solution can be expressed in terms of linear matrix relationships between transformed temperature and transformed heat flux vectors at the boundaries of the system. By this way, this solution is independent on these boundary conditions.

For 1D heat transfer in homogeneous and isotropic solid materials without internal heat source in a one-layer slab, the heat equation is given by:

$$\frac{\partial^2 T}{\partial x^2} = \frac{1}{a}\frac{\partial T}{\partial t}\left(T = T_0 \; for \; t = 0\right)$$

(Eq. 2.1)

The heat flux at any location *x* inside the slab is defined for any cross-section *S* as:

$$Q = -\lambda S \frac{\partial T}{\partial x}$$

(Eq. 2.2)

Applying Laplace transform to both temperature and flux, *θ(x,p)=L(T(x,t)) ; Φ (x,p)=L(Q (x,t)),* and consider the Laplace transforms *θ₁* and *θ₂* as the front (x=0) and rear (x=e) face temperatures, respectively, Φ_1 and Φ_2 as the corresponding heat fluxes shown inFigure 1, we obtain:

$$\begin{bmatrix} \theta_1 \\ \Phi_1 \end{bmatrix} = \begin{bmatrix} A & B \\ C & D \end{bmatrix}\begin{bmatrix} \theta_2 \\ \Phi_2 \end{bmatrix} = M\begin{bmatrix} \theta_2 \\ \Phi_2 \end{bmatrix}$$

(Eq. 2.3)

Where:

$$A = D = \cosh\left(e\sqrt{p/a}\right); B = \frac{1}{\lambda S\sqrt{p/a}}\sinh\left(e\sqrt{p/a}\right); C = \lambda S\sqrt{p/a}\sinh\left(e\sqrt{p/a}\right)$$

p is the Laplace transform of time; a is thermal diffusivity, λ is thermal conductivity, S the cross section, e is the sample thickness. The matrix M with the four coefficients A, B, C, D completely characterizes the external temperature response of heat flux.
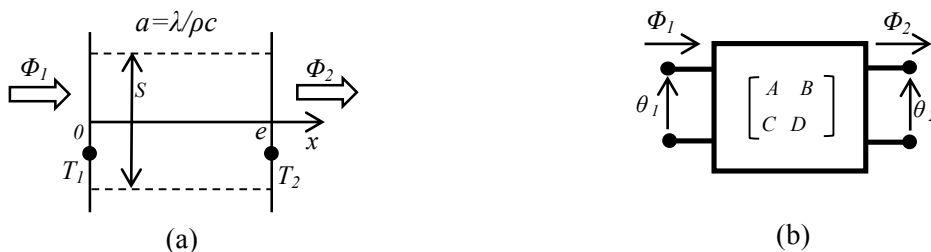

Figure 1: One layer slab in transient transfer: (a) geometry; (b) matrix representation

For multilayer medium, the global transfer matrix M_eq can be obtained by multiplying the matrices from each layer of medium *M₁, M₂...Mₙ*.

$$\begin{bmatrix} \theta_1 \\ \Phi_1 \end{bmatrix} = M_1 \cdot M_2 \ldots \cdot M_n \begin{bmatrix} \theta_2 \\ \Phi_2 \end{bmatrix} = M_{eq}\begin{bmatrix} \theta_2 \\ \Phi_2 \end{bmatrix}$$

(Eq. 2.4)

Semi-infinite condition and adiabatic boundary condition are considered and analysed.

Semi-infinite condition (a short time response)

For a semi-infinite medium, the value of thickness is infinite ($L = \infty$), so equation (Eq. 2.3) becomes

$$\begin{bmatrix} \boldsymbol{\theta_1} \\ \boldsymbol{\Phi_1} \end{bmatrix} = \begin{bmatrix} \mathbf{1} & \boldsymbol{z} \\ \mathbf{0} & \mathbf{1} \end{bmatrix}\begin{bmatrix} \boldsymbol{\theta_2} \\ \boldsymbol{\Phi_2} \end{bmatrix}, \quad \boldsymbol{z} = \frac{\mathbf{1}}{\boldsymbol{b}\sqrt{\boldsymbol{p}}}$$

(Eq. 2.5)

Adiabatic boundary condition

An adiabatic boundary condition of the rear face of wall is considered, that is $\Phi_2 = 0$, equation (Eq. 2.3) becomes:

$$\begin{bmatrix} \theta_1 \\ \Phi_1 \end{bmatrix} = \begin{bmatrix} A & B \\ C & D \end{bmatrix} \begin{bmatrix} \theta_2 \\ 0 \end{bmatrix}; \quad \theta_1 = \frac{A}{C}\varphi_1; \quad \theta_2 = \frac{1}{C}\varphi_1$$

(Eq. 2.6)

Actually, the temperature response in semi-infinite condition and in adiabatic condition performs the same trends in a short time (a few hours).

Therefore, with the heat flux of front face ($q_1(t)$) and thermal parameters of wall (λ,pc...), the temperature of both front face and rear face (T_1, T_2) can be estimated by the direct modelling, shown in Figure 2.
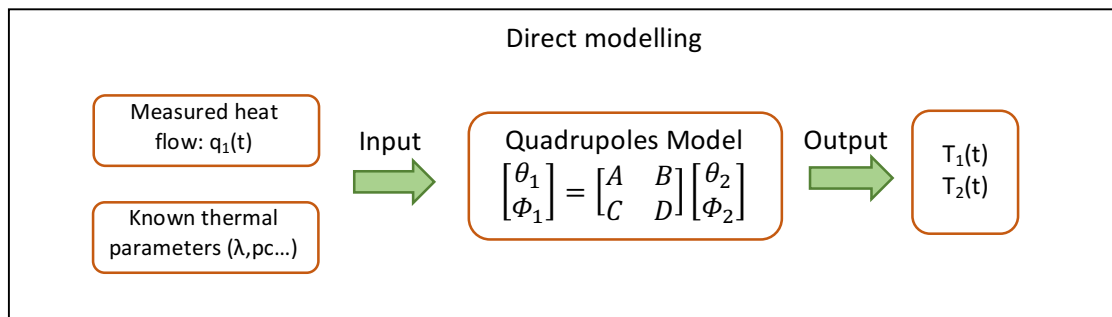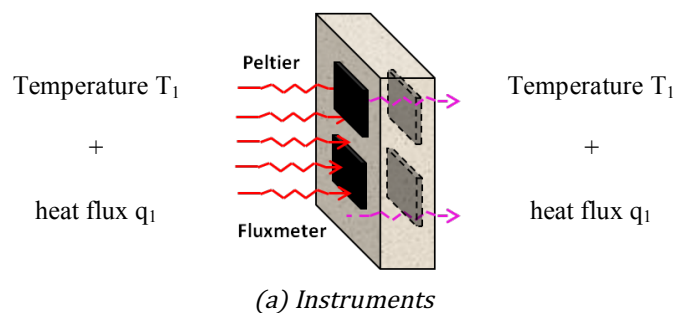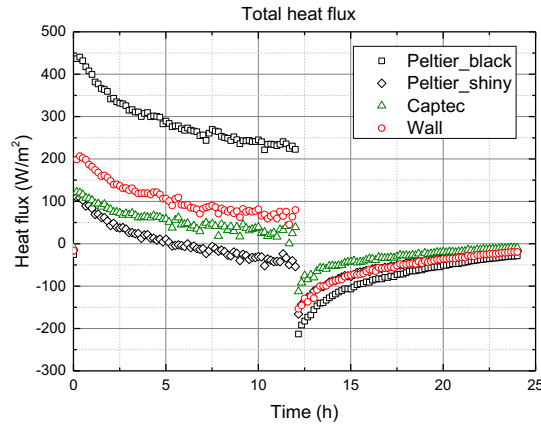

Figure 2: Wall direct modelling

Validation of Quadrupole model

Experiments were carried out in Nantes (IFSTTAR). The experimental set up and procedure are described in deliverable D2.3. Figure 3 shows the heat fluxes measured by Captec sensors and Peltier sensors. The heat flux of wall (q1) is calculated based on heat flux balance.

(a) Instruments

(b) Heat flux evolution

Figure 3: Heat fluxes (q₁) that measured by Captec sensor, Peltier sensor and heat flux of wall

The wall heat flux (q_1) and the suggested thermal parameters (values from the reference - thermal regulation 2012) are input to the direct modelling, and the estimated temperatures (T_1, T_2) are the outputs. Figure 4 (a,b,c) show the comparison between the simulated temperature and measured one. The front face is heated by the lamps and the rear face is at adiabatic boundary condition.
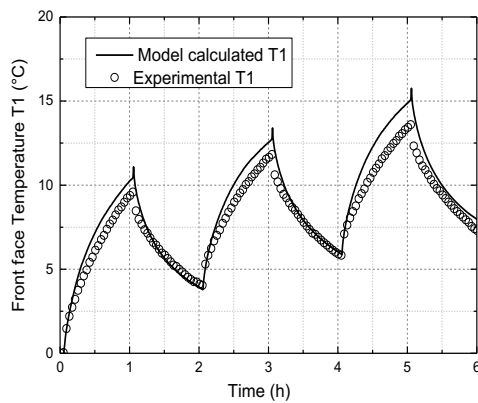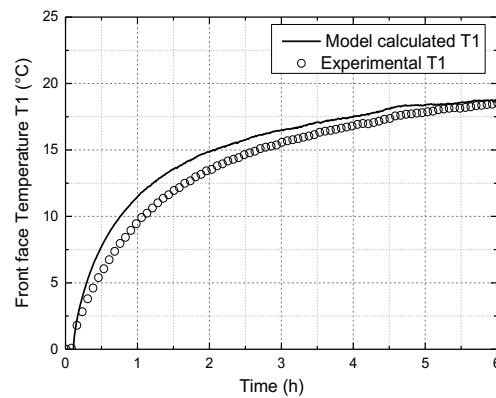
(a)   (b)
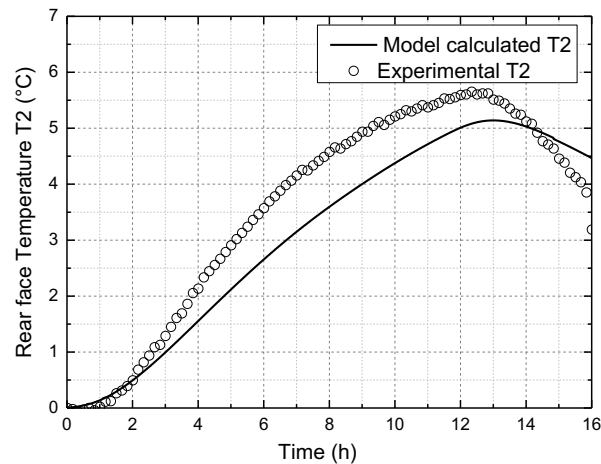
(c)

Figure 4: Comparison of model estimated temperature and experimental temperature (a) the front face temperature of a periodic heat signal (b) the front face temperature of a step heat signal; (c) the rear face temperature of a step heat signal

Figure 4 (a,b,c) show that the estimated temperature is in a good agreement with the experimental temperature by using reference values of thermal parameters, the difference between the two temperatures is less than 1 °C. The thermal quadrupole model has been validated in several works (M.Faye, Lartigue et Sambou 2015) (Braiek, et al. 2017). It is demonstrated that the thermal quadrupole model can predict the surface temperatures well in the heat transfer regime of thick walls.

2.2.3   Wall modelling: Finite differences model

2.2.3.1   THEORY OF THE APPLIED HEAT TRANSFER

The finite difference method hereafter exposed is applied to the heat equation according to experimental set-up described in D.2.3 and D.7.2 (Nuruzzaman 2013). This approach leads to a numerical code implemented in Matlab environment for UB group and in Python environment for Cerema group. This allows solving numerically the direct heat conduction transfer (VDI 2010).

In solid, non-transparent materials considered in the present work, heat transfer only occurs through conduction without heat generation. In thermal studies for thermo-physical properties estimation, the 1D unidirectional transfer is considered. In this case, the heat transfer is determined by the heat equation in its simplest form (Eq. 2.7). Analytical solutions to this equation exist for the least complex cases but for larger applications one needs numerical simulations. The finite difference method as explained further in this section allows simulating the temperatures within the studied sample or wall.

$$\frac{\partial T}{\partial t} = a\frac{\partial^2 T}{\partial x^2}$$

(Eq. 2.7)

Where a(m²/s) is thermal diffusivity.

2.2.3.2   NUMERICAL HEAT TRANSFER MODELLING: DISCRETISATION-IMPLICIT SCHEME

In the majority of the cases numerical modelling proves crucial to solve this type of heat conduction problem. The finite difference method is adapted to our unidirectional case study. Once programmed, it

allows the resolution of the heat transfer direct problem. It calculates the temperatures at the chosen nodes after the field under study has been discretized through an unconditionally stable implicit scheme (refer to Figure 5: in a simple case, the sample could be made of only one layer). The nodes j (j = 1, ..., M) are separated by a Δx distance. They represent the spatial variable x where the temperature will be simulated. In the same way, the testing time i was discretized (i = 1, ..., N) with a Δt time step.

The input data of the numerical model are the temperature fields measured at the boundaries "a" and "b" and at the interfaces. The temperature fields recorded at the extremities "a" and "b" of the sample $T_{exta}(i \cdot \Delta t)$ and $T_{extb}(i \cdot \Delta t)$ are the boundary conditions of the Dirichlet type (known time function). This type of boundary conditions makes it possible to have not to rely on the determination of the convection and radiation coefficient h.

When the test is being carried out, the system is assumed to be in an apparent stationary state. In these conditions the initial temperature field of the sample $(T_{ini}(j \cdot \Delta x))$ to be characterized is determined by interpolation between known initial nodes' temperatures (refer to Figure 5).

The implicit scheme of the finite difference method applied to (Eq. 2.7) leads to its time and space discretization as written in (Eq. 2.8):

$$\frac{T_i^{n+1} - T_i^n}{\Delta t} = a_i \frac{T_{i-1}^{n+1} - 2T_i^{n+1} + T_{i+1}^{n+1}}{\Delta x^2} + o(\Delta t, \Delta x^2)$$
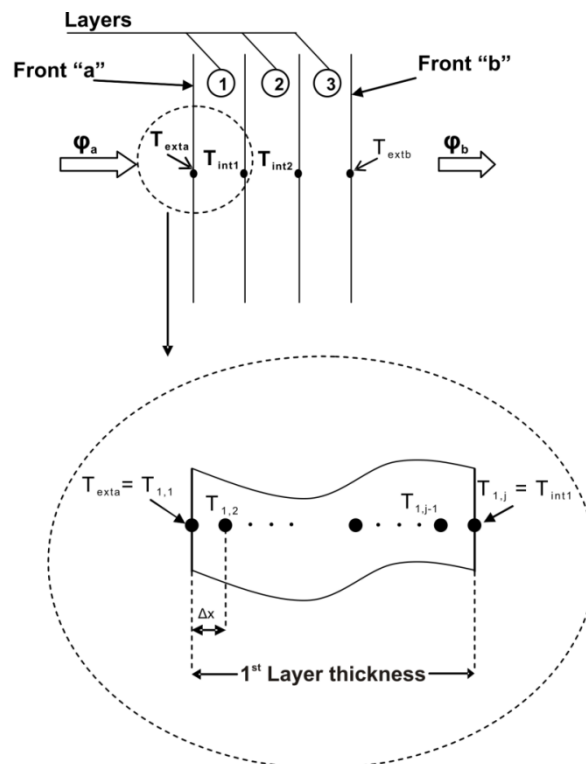
(Eq. 2.8)

Figure 5: Configuration of the tested sample and detailed discretization.

The last equation is equivalent to equations (Eq. 2.9) and (Eq. 2.10). The chosen scheme is unconditionally stable and converging independently of "r_i" values which are constant for each layer.

$$r_i T_{i-1}^{n+1} - (1 + 2r_i)T_i^{n+1} + r_i T_{i+1}^{n+1} = -T_i^n$$

(Eq. 2.9)

$$r_i = \frac{a_i \Delta t}{\Delta x^2}$$

(Eq. 2.10)

Expanding the last equation (Eq. 2.10) one can find:

$$\begin{cases} T_0^{n+1} = T_a = T_{exta} & for\ i = 0 \\ -r_i T_{i-1}^{n+1} + (1 + 2r_i)T_i^{n+1} - r_i T_{i+1}^{n+1} = T_i^n & for\ i = 1, \dots, M-1 \\ T_M^{n+1} = T_b = T_{extb} & for\ i = M \end{cases}$$

(Eq. 2.11)

Writing the matrix form of the above equation system, one can find:

$$\begin{pmatrix} 1 & 0 & 0 & & & & \\ -r_1 & 1+2r_1 & -r_1 & \cdots & & 0 & \\ 0 & -r_2 & 1+2r_2 & & & & \\ & \vdots & & \ddots & & \vdots & \\ & & & 1+2r_{M-2} & -r_{M-2} & 0 \\ & 0 & \cdots & -r_{M-1} & 1+2r_{M-1} & -r_{M-1} \\ & & & 0 & 0 & 1 \end{pmatrix} \begin{pmatrix} T_0^{n+1} \\ T_1^{n+1} \\ \vdots \\ \vdots \\ T_{M-1}^{n+1} \\ T_M^{n+1} \end{pmatrix} = \begin{pmatrix} T_a \\ T_1^n \\ \vdots \\ \vdots \\ T_{M-1}^{n+1} \\ T_b \end{pmatrix}$$

(Eq. 2.12)

Where the matrix is called "R" is the system matrix.

Using the finite difference method applied to the heat equation makes it possible to have a matrix system such as $R \cdot \theta = B$ where R is the matrix describing the system. Its terms are determined by the thermo-physical properties of the material (thermal conductivity λ and volumetric heat capacity ρC) and by its geometrical parameters. θ is the temperature vector to be calculated at a given instant "*t*" and B is defined from the temperature vector known at "*t-1*" and from the boundary conditions.

The energy balance and the application of the implicit scheme at the interfaces make it possible to compute the temperatures. The volumetric heat capacity at one interface is equal to the mean of the volumetric heat capacities in the two layers limiting the interface.

In the present work, the contact resistance at the interfaces is considered negligible in comparison to the thermal resistance of the different layers. Characteristics like thickness, thermal conductivity and quality of the surface make it possible to neglect the contact resistance in this numerical model for the range of the tested construction materials. Naturally, concerning conductive or thin layers materials, this hypothesis would need to be adapted. The above developed numerical model for direct heat transfer analysis is coded step by step, following the implementation of the finite difference method on Matlab or Python mathematical calculus software. This allows simulating the spatiotemporal temperature evolution in the wall.

2.2.3.3   MODEL VALIDATION: NUMERICAL SIMULATION VS ANALYTICAL SOLUTION.

The considered test is transient with boundary conditions: $T_{exta} = T_a = T_{extb} = T_b = 0°C$, and initial temperature as shown on Figure 6. In fact, the initial temperature inside the material will decrease until $0°C$ through the thickness of the material and the system will reach the stationary state.

The validation of the above exposed numerical simulation has been done by comparing its results with those of an analytical solution to direct heat transfer problem. (Eq. 2.13) shows the analytical solution for the problem (Eq. 2.1). It allows in this study case for temperature calculation "T_{exact}" through the material thickness "x" and during the test time "t".
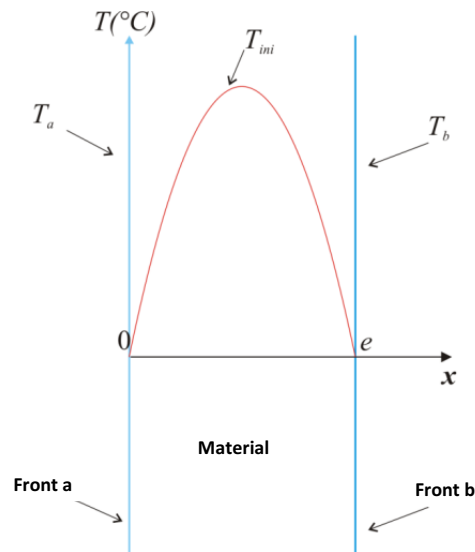
Figure 6: Studied case for finite differences for heat transfer model validation

$$T(x,t) = \sum_{n=1}^{\infty} \left(b_n \sin(\frac{n\pi x}{e}) \exp\left(\frac{-an^2\pi^2 t}{e^2}\right) \right)$$

(Eq. 2.13)

Where e is the material thickness and b_n solution coefficient calculated using initial and boundary conditions.
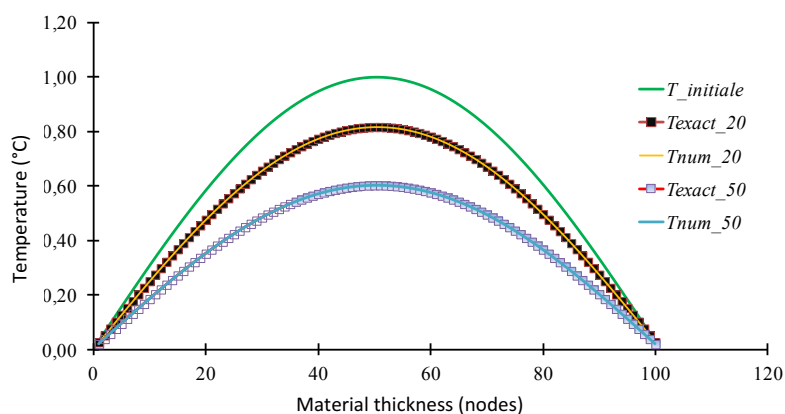
Figure 7: Finite difference model validation: numerical solution VS analytical solution

Numerical solution "T_{num}" is compared to analytical "T_{exact}" at two points of the transient test: t=20s and t=50s (Figure 7). In fact, the comparison was made for all the time steps and the conclusions were the same. The numerical solution curve and the analytical one are hardly distinguishable which means that the numerical model is reliable. The cumulated differences between the two calculated temperatures are

lower than 10^{-8} °C. Thus, the developed model based on finite difference applied to the direct heat transfer problem has been validated for the actual study case (Derbal 2014).

2.2.4 Detailed modelling: Solene-Microclimat – thermal envelope model for defects integration

The numerical developments concern the modelling of defects in the envelope of building when taking into account the local climate (detailed external conditions) in the assessment of building actual efficiency. For this assessment, we use Solene-microclimat which is dedicated to modelling urban microclimate and building thermal behaviour (Figure 8). The first micro climatic potentialities of this tool had been developed through different works at the CERMA laboratory (Vinet 2000) (Robitu 2005).This tool can model the thermos-radiative balance of an urban scene. Also, the possibility to use a CFD (computational fluid dynamics) tool to calculate the air flow for the internal or external air exchanges of buildings was developed in successive studies (Robitu 2005). The Solene-microclimat thermo-radiative model, its validation and coupling with Code-Saturne CFD model have been presented in (Malys 2012).The BES (Building Energy Simulation) coupling was presented in detail by (Bouyer, Inard et Musy 2011); it consists of a sub-model for SOLENE and is based on a multizone building nodal network model, whose nodes correspond to building floors. This part has not been validated yet. This step will require monitoring a building. The thermo-radiative part of the model has been validated (Hénon, Mestayer et Groleau, et al. 2011), as well as the green wall model (Malys 2012). To complete the validation, comparisons for ground, wall and roof models were realized. For this purpose, the measurement data acquired during FluxSap[1] experimental campaign have been used (Mestayer, et al. 2011). The measurements have been performed around Pin Sec, a district located in the "second ring" between the 19[th]century boulevards and the rim speedway, in Nantes (FRANCE).

To summarize, SOLENE-microclimat (Musy, et al. 2015) was first developed for an urban amenity assessment, with the possibility to take into account (Figure 8):

- Radiative transfers, including long-wave radiation;
- Conduction and storage in walls and soils;
- Airflow and convective exchanges;
- Evapotranspiration from natural surfaces like vegetation and water ponds or humidification systems;
- Building energy consumption.

2.2.4.1 MODELLING APPROACH FOR THIS PROJECT

The whole model used in this section to carry out simulations is a coupling between a new developed thermal model and the existing radiative and thermo-radiativefunctions of Solene-microclimat representative of the environment.

In this section, the radiative and convective transfers, the conduction and storage in soils and buildings will be considered. A real 3D geometry is considered, which comes from the 3D vectorial description of the BDTopo. The developed building model is presented in the next part. The actual geometry, the experimental site and the monitoring set-up are presented in deliverables D 3.2 and D 7.2.
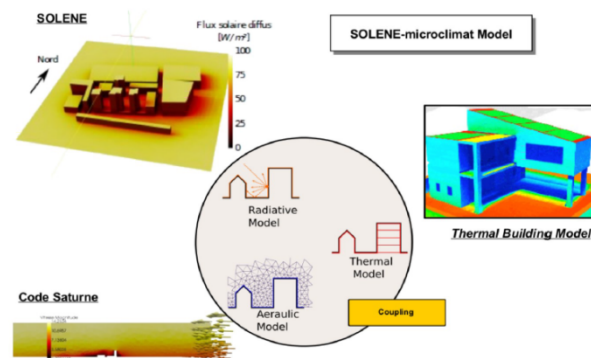
---

[1] http://www.meteo.fr/icuc9/presentations/NOMTM/NOMTM7-4.pdf

Figure 8: SOLENE-Microclimat

2.2.4.2 DEVELOPMENT OF A BUILDING THERMAL MODEL FOR INTEGRATING THE DEFECTS

Among the thermal properties of the walls, the choice of the U-values has a high impact on the simulation results (Spitz, et al. 2012) (Borderon, et al. 2013) (Asdrubali, et al. 2014) and the ISO E. 6946 (ISO 2007) showed that U-values can be underestimated up to 30% by calculation. For both retrofit and new buildings, self-inspection tools can be useful to detect the structural defects. Many buildings suffer from defects in the envelope, such as missing insulation, thermal bridging and cracks. During a walk-through thermography inspection, (Fox, Goodhew et De Wilde 2016) calculated that conductivity defect (missing or damaged insulation and cold bridging) represented a proportion of 37.2 % of thermally significant building defects. At the material scale, (Aissani, et al. 2016)showed that the thermal resistance of insulations is significantly affected by all kinds of defects (crush, groove, sheath passage and opening). They showed that insulation panels were found to lose more than 36 % of their performance when openings represent only 0.5 % of the total insulation volume. Missing insulation and cracks are, for example, observed for constructions using prefabricated modules for panel buildings (Sztanyi 2015).

Although these types of defects have an impact on the global performance of the envelope, in literature, they are commonly studied at a small scale and not considered at a building scale surrounded by a realistic environment.

In order to reduce the energy performance gap between buildings as designed and as-built, the construction defects need to be properly located and considered in the whole simulation process.

In this work, we focus on the impact of defects on the thermal behaviour of a building surrounded by a realistic environment in actual operational conditions. In this view, we implemented an envelope model that has the advantage to consider two kinds of defects:

- Defects effective on the entire envelope, such as materials with different thermal properties than initially planned during the design stage.
- Defects effective on a part of the envelope, such as a localized lack of material, in order to deal with missing or damaged insulation, groove, sheath passage and openings.

In the following sections, the dynamic building thermal model is presented. The envelope model is completely new and is adapted to the integration of the above-mentioned defects. The validation process of the envelope model is presented afterwards. Firstly, the thermal wall model response is compared to an analytical solution. Then, the building envelope model comparison to TrnSys® is reported and a first comparison with the model is shown. Finally, the impacts of two defects are presented.

2.2.4.2.1 Description of the building thermal model

A new thermal model is developed here to answer to the aim of this work. The current thermal envelope model which could be coupled to Solene-microclimat was the model of (Bouyer, Inard et Musy 2011). Unfortunately, the latter model is not adapted to a refined discretization of the walls as it is a 1R2C wall model. Also, integration of a defect such as a lack of insulation cannot be considered at a local scale. The impact of the wall orientations on the inside surface temperatures is not considered either. This model development is interesting for energy calculations of a building surrounded by a realistic environment but not for a detailed study of the envelope. The outputs of the current model and of the new model appear in Table 1. We decided to develop a new thermal model and not to use commercial software as TrnSys or EnergyPlus as these tools cannot be coupled easily to Solene-microclimat and they do not allow refining the spatial discretization of walls as needed for the study of defects.

The new model can represent the dynamic behaviour of a single building of any shape using a multizone approach, where each level is a zone. Internal gains and air exchanges are considered. Heating loads are calculated as well as the air and radiant temperatures for each floor. The external surfaces temperatures are calculated for each mesh of the building, as we consider discretized boundary conditions. At the inside and for each level different surface temperatures are calculated for the envelope. In this thermal model, we refined the spatial discretization of the walls. We implemented a more detailed wall model in order to have a spatial discretization through the walls and to have at least one inside surface temperature per wall and per level. Now we no longer connect directly the outside surface nodes to one inside surface node but to a larger number of inside surface nodes, so that we can have several inside surface temperatures for different wall orientations. The new model provides more outputs as shown in Table 1. Local defects can be added and the inside surface temperature distribution can be calculated, which was not the case before. The wall model uses a finite difference method described in section 2.2.3.2. The spatial discretization of the wall is flexible. For example, a mesh generator can generate finer meshesin the area where the defect is localized. On the outside of the building envelope spatial discretization follows a Gmsh[2] unstructured meshing which is also used for all the radiative calculations of Solene-microclimat. The meshes generated are named triangles and a set of triangles belonging to a same type of surface is called a face. On figure 18, you can see triangles and in white the edges of the faces.

The building model is coupled to Solene-microclimat, which has the advantage to represent the building shapes (3D geometry), the detailed external radiative exchanges, the conduction and storage in soils and the climatic environment. Between the building model and Solene-microclimat we implemented a weak coupling (Figure 9). At each time step the short-wave radiation after inter-reflection is calculated for each mesh of the urban scene. Then, the building model is run. The outside surface temperatures calculated with the building model are used in Solene-microclimat to calculate all the long wave and heat exchanges between the modelled building and the soil and the other buildings of the small allotment. Finally, all the allotment heat flows and temperatures are obtained for this time step (Figure 9).

---

[2]A three-dimensional finite element mesh generator with built-in pre- and post-processing facilities

Input

✓ **3D Model** of the urban scene
✓ **Boundary conditions** (Radiation, Outside temperature, Wind, sky temperature or Downward flow)
✓ For the building and the surrounding :
   Thermal data of the wall layers and windows
   Optical characteristics
✓ **SOLENE** : short wave radiation after interreflections for the simulation period

Calculation
1D Heat equation in finite differences n.R(n+1).C **Balance equations** at the surfaces : φ cond + φ conv + φ rad = 0 **Air balance equation**

ti

| **SOLENE** : balance equation of the scene's triangles |

t$_{i+1}$

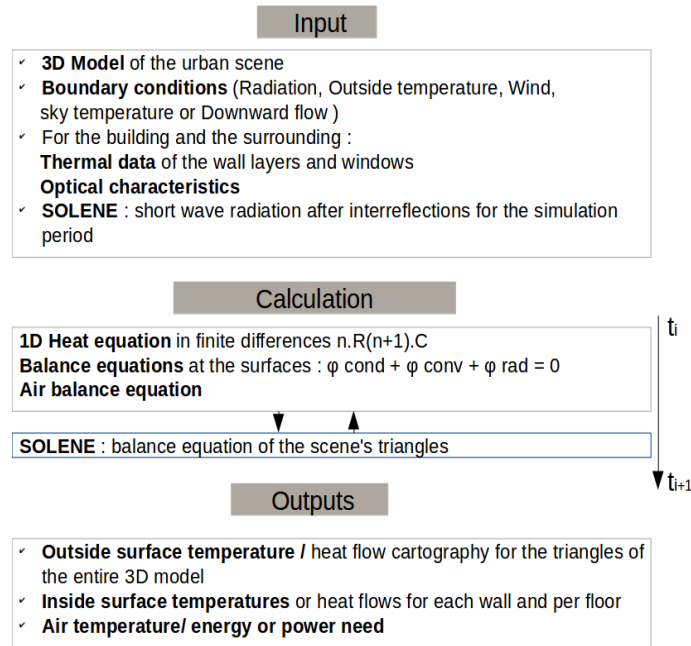| Outputs |
| --- |
| ✓ **Outside surface temperature /** heat flow cartography for the triangles of the entire 3D model
✓ **Inside surface temperatures** or heat flows for each wall and per floor
✓ **Air temperature/ energy or power need** |

Figure 9: Calculation flow of the new thermal model coupled to Solene-microclimat.

The same is done for the roofs and windows. But for the floors, we do not apply a two-dimensional discretization.

Between each level the nodes located on the flooring are the connections between the levels. For each mesh located on the building either at the inside or outside, the heat equation is solved to get the mesh's temperature, T [K]:

$$\rho c V \frac{\partial T}{\partial t} = \varphi_{\text{conv}} + \varphi_{\text{cond}} + \varphi_{\text{SW}} + \varphi_{\text{LW}}$$

(Eq. 2.14)

Table 1: Outputs of the models

Outputs of the first model (Bouyer et al. (2012))	Outputs of the new model
For one level	For one level
• 1 air and radiant temperature • 1 inside surface temperature for all the envelope walls • N Outside surface temperatures, where N is the number of meshes on the building envelope • 1 floor temperature • 1 ceiling temperature • Heating or cooling load	• 1 air and radiant temperature • Nw or more inside surface temperatures, where Nw is the number of walls • Nw or more node temperatures through the wall, where Nw is the number of walls • N Outside surface temperatures, where N is the number of meshes on the building envelope • Temperature profiles through the walls • 1 floor temperature • 1 ceiling temperature • Heating or cooling load

Here φ_{conv} is the convective flow, φ_{cond} is the conduction flow, φ_{SW} is the short-wave radiation flow and φ_{LW} is the long wave radiation flow. The density of air ρ [kg/m^3], the specific heat capacity c [J/kg$K$] and V [m^3] the volume of the zone. The convective heat flow follows this equation:

$$\varphi_{conv} = hconv\ S\ (T_S\ -\ T_{airi})$$

(Eq. 2.15)

T_{airi} is the outside or inside air temperature, T_S is the surface temperature, S is the surface and h is constant through the time for the inside of the building (6.1W/m²K for the ceiling, 1.6 W/m²K for the floor and 4.1W/m²K for the walls). For the outside, h_{conv} changes in time, as a function of the wind speed v [m/s] (Jayamaha, Wijeysundera et Chou 1996):

$$hconv = 5.85 + 1.7\ v$$

(Eq. 2.16)

The conduction between two neighbouring meshes i and i+1 in the wall is given by:

$$\varphi_{cond} = k_{i,i+1}(T_i - T_{i+1})$$

(Eq. 2.17)

With

$$k_{i,i+1} = \frac{S_{i,i+1}}{\frac{\delta_i}{2\lambda_i} + \frac{\delta_{i+1}}{2\lambda_{i+1}}}$$

Here T [K] is a node temperature, k[W/K] is the thermal conductance, S [m²] is the surface, λ [W/mK] the conductivity, δ the thickness [m] between the two nodes, and i the number of the mesh.

φ_{SW} [W/m²] is the short-wave radiation flow. At the inside of the building only the floor receives radiation.

$$\varphi_{SW,in} = \alpha S_w \tau E_{SW}$$
(Eq. 2.18)

Here, α is the absorptivity coefficient of the wall coating, Sw is the wall surface, τ is the solar transmission through the glaze window and, $E_{SW} \left[\frac{W}{m^2}\right]$ is the short-wave radiation after inter-reflection using the radiosity method. $\varphi_{LW} \left[\frac{W}{m^2}\right]$ is the longwave radiation flow. For a mesh exposed towards the outside environment, the long wave exchanges are given by:

$$\varphi_{LW,e,tri} = S_{tri}\varepsilon_{tri}h_r \left(F_{sky \to tri}(T_{Sky} - T_{tri}) + F_{sc \to tri}(T_{sc} - T_{tri})\right)$$

(Eq. 2.19)

Here, $h_r = \sigma(T_{Sky} + T_{tri})(T_{Sky}^2 + T_{tri}^2)$ is rounded to 5 W/m²K. S_{tri} is the surface of the mesh[m²] and ε_{tri} the emissivity of the mesh. T_{sc}[K] is the temperature of a mesh of the scene, T_{tri} [K] is the temperature of a mesh of the building and T_{Sky} [K] the temperature of the sky. $F_{sky \to tri}$ and $F_{sc \to tri}$ are the shape factors between the considered mesh and the sky and the shape factor between a mesh of the urban scene, a mesh of the building and the sky vault. These shape factors are directly calculated by Solene-microclimat. This allows to have realistic long wave exchanges between the studied building and the surrounding. For the inside of the building, the long wave exchanges for a surface are given by:

$$\varphi_{LW,i,f} = S_f h_r \sum_{j \neq f} \varepsilon_f F_{j \to f}(T_f - T_j)$$

(Eq. 2.20)

Here S_f [m²] is the surface of the face, h_r the radiative coefficient rounded to 5 W/m²K, ε_f the emissivity, $F_{j \to f}$ the shape factor between faces, T_f the temperature of the face and T_j the temperature of another face. The finite difference equation for a node in the wall is given by:

$$\rho c V \frac{T_i^{t+\Delta t} - T_i^t}{\Delta t} = k_{i,i+1}\left(T_i^{t+\Delta t} - T_{i+1}^{t+\Delta t}\right) + k_{i,i-1}\left(T_i^{t+\Delta t} - T_{i-1}^{t+\Delta t}\right)$$

(Eq. 2.21)

If the mesh is located on a surface:

$$\rho c V \frac{T_S^{t+\Delta t} - T_S^t}{\Delta t} = k_{i,i+1}\left(T_S^{t+\Delta t} - T_{i+1}^{t+\Delta t}\right) + h(T_S - T_{airi}) + \varphi_{SW}^{t+\Delta t} + \varphi_{LW}^{t+\Delta t}$$

Finally, the air temperature is given by:

$$\rho C_p V \frac{T_{air}^{t+\Delta t} - T_{air}^t}{\Delta t} = \sum_f h_{conv} S_f\left(T_{airi}^{t+\Delta t} - T_f^{t+\Delta t}\right) + Q + I$$

(Eq. 2.22)

Where Q [W] is the heating or cooling load, I [W] is the loss due to the infiltration rate and T_{airi}[K] the inside air temperature for a level. In this work, we consider I = 0.

This can be summarised as a matrix problem:

$$\mathbf{M} \begin{pmatrix} \mathbf{T}_{tri,o}^{t+\Delta t} \\ \vdots \\ \mathbf{T}_i^{t+\Delta t} \\ \vdots \\ \mathbf{T}_{f,i}^{t+\Delta t} \\ T_{air}^{t+\Delta t} \end{pmatrix} = \begin{pmatrix} S_{tri,o} \\ \vdots \\ A_i \mathbf{T}_i^t \\ \vdots \\ S_{f,i} \\ A_{air} \mathbf{T}_{air}^t \end{pmatrix}$$

(Eq. 2.23)

Where $A = \frac{\rho c V}{\Delta t}$ and $S_{f,i} = A_{f,i} \mathbf{T}_{f,i}^t + \varphi_{LW,i,f}$ with:

$$S_{tri,o} = A_{tri,o}.\mathbf{T}_{tri,o}^t + S_{tri}\varepsilon_{tri}h_r\left(F_{sky \to tri}T_{Sky}^{t+\Delta t} + F_{sc \to tri}T_{sc}^{t+\Delta t}\right) + \varphi_{SW,o}^{t+\Delta t}$$

(Eq. 2.24)

M represents the matrix coupling the calculated temperatures. The inversion of the matrix allows the calculations of all the temperatures at the time step t + Δt using an implicit numerical resolution method which is unconditionally stable.

2.2.4.3   VALIDATION OF THE BUILDING ENVELOPE MODEL

As explained in the introduction, several parts of Solene-microclimat have been validated, separately from the building model. The new envelope model will follow a validation process introduced here. This is an important evolution as until now no thermal building model coupled to Solene-microclimat was validated or compared to an analytical solution or commercial tool.

2.2.4.3.1 Comparison to an analytical solution

At first, the thermal wall model response is compared to an analytical solution. The thermal wall model is a direct model based on the finite method presented in Section 2.2.3.2. The analytical solution considers a lateral and lower adiabatic limit and a superior constant temperature $T_i = 300$ K. The initial temperature is $T_0 = 270$ K. The temperature time evolution for depth z is:

$$T(z, t) = T_i + (T_0 - T_i)\mathrm{erf}\left(\frac{z}{2\sqrt{a.t}}\right)$$

(Eq. 2.25)

Where $a = \frac{\lambda}{\rho C}$ is the material thermal diffusivity.

Figure 10 presents the results for two points calculated at depths $z_1 = 3.3$ mm and $z_2 = 166$ mm. We can observe that the response of the model, in terms of temperature shows good agreement with the analytical solution.
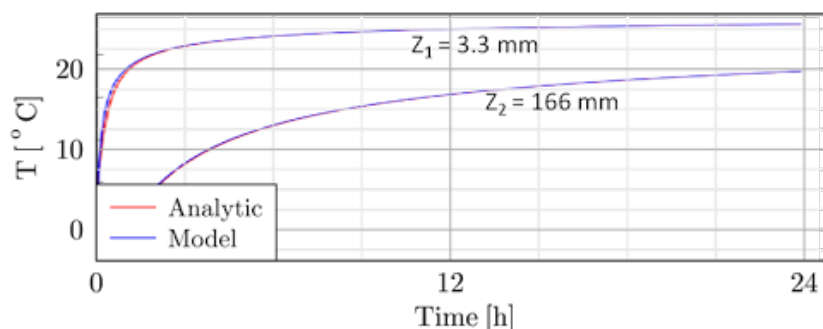

Figure 10: Wall temperature at different depths compared to an analytical solution

2.2.4.3.2 Comparison to TRNSYS

Secondly, the building model is compared to TrnSys calculation. For these simulations, a simple single building geometry was chosen without surrounding buildings. A 3-level cubic building was considered. The building was 30m in depth, 30m in large and 9m in height. For each floor and wall a 25 m^2double-glazing window was considered. The selected weather data are shown in Figure 11. The following assumptions were made for both TrnSys and the new building thermal model:

- We have taken the same internal and external convective coefficients;
- We have assumed that the ground temperature was constant and equal to 15 °C;
- we have considered the same transmission coefficients of the windows for both direct and diffuse radiation;
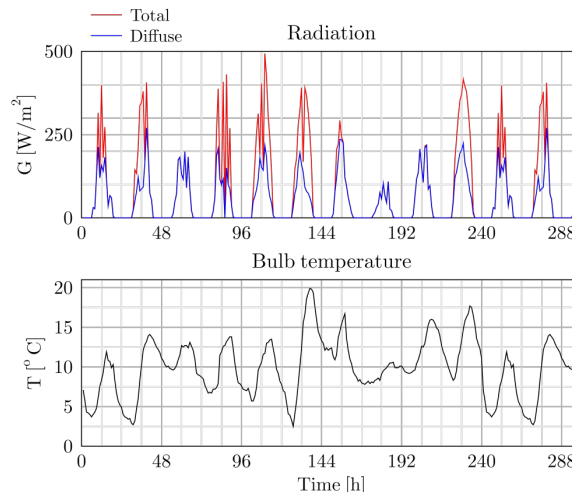- We have neglected the air infiltrations.

Figure 11: Weather data considered for the simulations

Due to simulation run time constraints, we have matched in the new model, for each wall the nodes located on the outside of the envelope to a single surface node exchanging with the inside of the level. That is for example, for 5 external walls we will have 5 inside surface temperatures for the walls.

However, the radiation distribution for the two models is different. Solene-microclimat considers the sky vault as a source of diffuse energy with a non-uniform luminance distribution. TrnSys does not follow this assumption. For free floating conditions, we have compared the air temperatures for the different floors. The difference between TrnSys and the new models can reach up to 0.8 °C and is most of the time between -0.5 °C and 0.5 °C (Figure 12).

The highest differences are observed for the last floor, probably due to the modelling differences for the long wave exchanges between the sky and the building.

For winter conditions with a constant temperature of 19°C, the air temperatures of the floors are quite close for both models. Differences between 0 and 0.8 °C are observed for the ground floor. The heating energy difference obtained for the ground floor represents 0.5 %, which is a very low difference. For the second floor, the air temperature difference is between 0 and 0.9°C and the heating energy difference is of 3.6 %. For the last floor the air temperature difference is again between 0 and 0.9 °C and the heating energy difference is of 4%.

To conclude, we can consider that the new building thermal model is validated since the global tendency of this model is acceptable, when compared it to either the analytical solution or TrnSys in free floating conditions or winter conditions (Figure 13).

2.2.4.4   APPLICATION: IMPACT OF THE DEFECTS

In this section, we analyze the impacts of two kinds of defects relating to an exterior insulation:

- A different insulation than initially planned: the range of conductivity can be different and also the thickness.
- A lack of insulation.

For these studies, we have considered a 5-level building which is located in Nantes. This building is surrounded by 7other buildings. This experimental site is described in detail in deliverable D.2.3. For the simulations, we considered only the central building and the four surrounding buildings (Figure 14).

During the simulation period, a set point temperature of 19°C was kept constant. The external walls are composed, from the outside towards the inside, of: 1 cm coating, an external thermal insulation, 25 cm of concrete and 1.3 cm of plaster. The roof is considered to have the same thermal properties and thicknesses as the walls. The ground slab is composed of a 10 cm external insulation and 30 cm of concrete. Each floor is composed of 15 cm of concrete and a 1cm parquet floor (Table 2). The thermal characteristics are given below:

Table 2: Envelope thermal properties

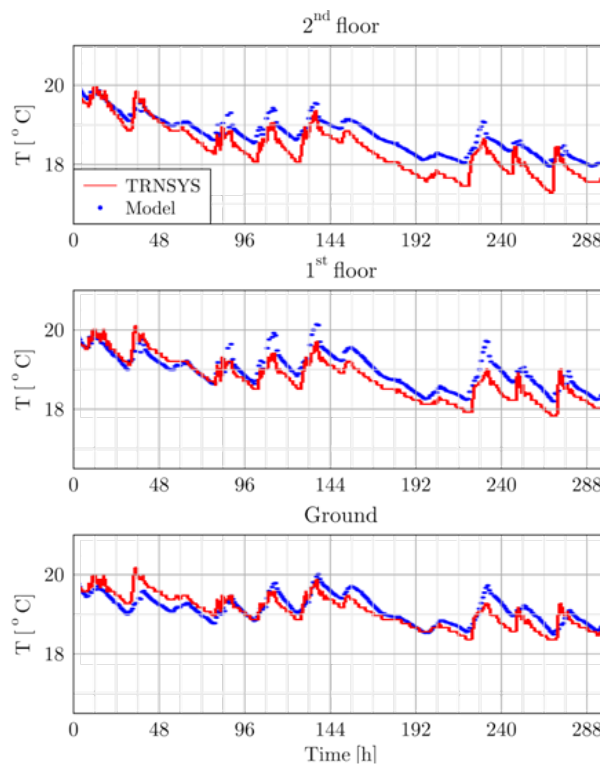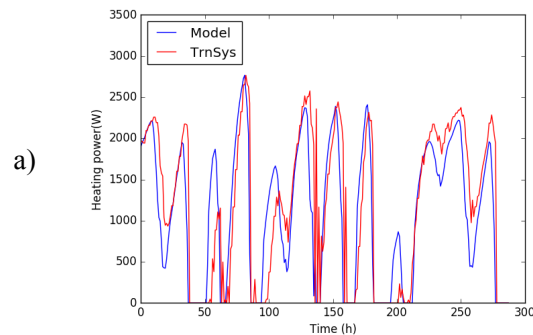|	Coating	Insulation	Concrete	Plaster	Parquet
Conductivity (W/mK)	0.75	0.032±0.012	1.33	0.42	0.13
Density (kg/m^3)	1450	30	2300	1200	1880
Heat capacity (J/kgK)	1000	1000	880	850	400

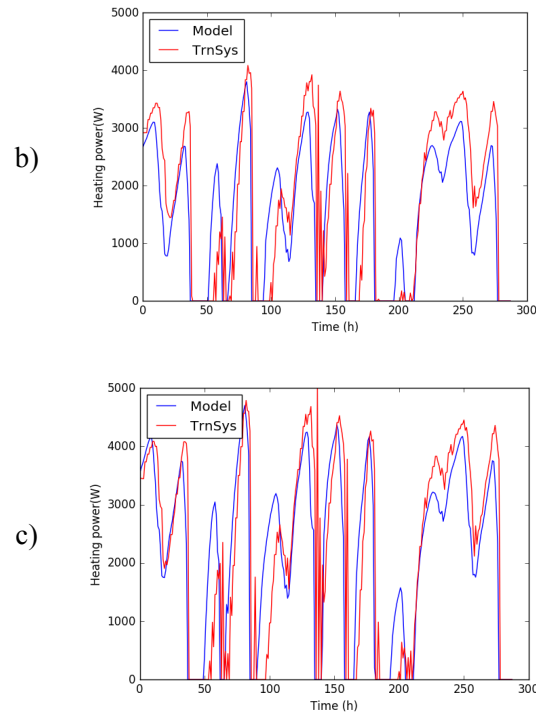*Figure 12: Air temperature of TrnSys and the developed model*

a)

b)

c)

Figure 13: Heating power of TrnSys and the developed model for: a) the ground floor, b) the first floor, c) the second floor
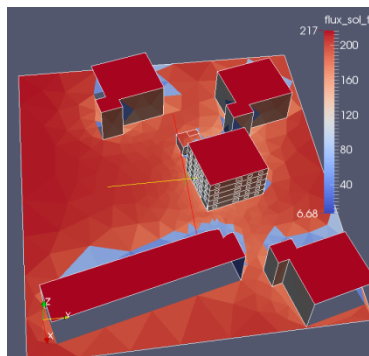

Figure 14: The urban area and the total solar radiation distribution

2.2.4.4.1 Impact of conductivity and insulation thickness differences at a whole building scale

The cases treated referring to the first type of defects are: a material with different properties than initially planned during the design stage, a material with different thickness than initially planned or a completely new insulation type with a different property and thickness. Simulations have been carried out to check how these defects influence the heating load. Here, the changes are made on the entire building envelope. The aim is to compare to a reference or required power associated with an uncertainty range due to the impact of the defects. The reference is simulation S2 (Table 3): we consider that the required exterior insulation for the rehabilitation corresponds to 18cm thick woollen insulation, the conductivity of which is supposed to be 0.03 W/m.K. Simulation 1 considers a defect where the thickness of the insulation might have changed. To consider the impact of both changes in thickness and in conductivity for a same type of insulation, simulations S3 to S6 were done. Finally, simulations 7 to 10 were done for a defect where the insulation type is different than the one planned. Here, two insulation types were considered: wool and polyurethane. The simulations are summarized in Table 3.

For the entire envelope surface either the conductivity or the thickness was changed but not the heat capacity and density. The thicknesses were chosen according to the most common use for external insulation in France. The conductivity and thickness intervals have been chosen according to the information found in a construction report[3].

Table 3: Tested thicknesses and conductivity values

Simulation	S_1	S_2	S_3	S_4	S_5	S_6	S_7	S_8	S_9	S_{10}
Thickness [cm]	15	18	15	18	15	18	10	14	10	14
Conductivity [W/mK]	0.03	0.03	0.04	0.04	0.045	0.045	0.022	0.022	0.03	0.03
Insulation type	Wool						Polyurethane			

No global sensitivity study had been done before studying the impact of the thickness and the conductivity because a large number of studies showed that among the variables identified on a building the most influential in sensitivity analysis are the U values (Borderon, et al. 2013) (Spitz, et al. 2012).

The uncertainty range relative to the woollen insulation is presented as the blue areas on Figure 15. The uncertainty range linked to the polyurethane is presented in brown (Figure 16). The black curve represents the reference simulation S2.

We can see on Figure 15 and Figure 16 that the mean heating power between the levels is different. For the ground floor and last floor, the heat demands are higher. For these cases, the levels have a larger envelope surface in contact with low temperatures. The other levels which are in contact with an upper and lower floor have lower heat losses and therefore lower heat demands. These observations show that the coupling between floors has an impact on the powers but also on the simulation range. The air temperature during the day can overpass the set point temperature due to the solar gains. This is not observed at the ground floor.

Concerning the impact of conductivity and thickness we see that the simulation ranges in blue and brown are higher for the ground floor and the last floor due to a larger temperature gradient between the inside and outside. The impact of conductivity and thickness of either the woollen insulation or polyurethane on the reference simulation S2 seem to be similar, unless for the ground and first floor (Figure 15 and Figure 16). In terms of energy, we have quantified the maximal absolute difference between the maximum and minimum energy obtained with the simulations of each type of insulation and with respect to simulation S2 (Table 4). We observe, as expected, important differences for all floors and all types of insulation, between 18.9 and 63%.

---

[3]GUIDE FOR INSULATING MATERIALS for efficient and sustainable insulation (in French): http://www.energivie.info/sites/default/files/documents/energivie_guide_isolants_24p_bd_6.pdf

Table 4: Simulation energy differences (normalized by the reference heat energy)

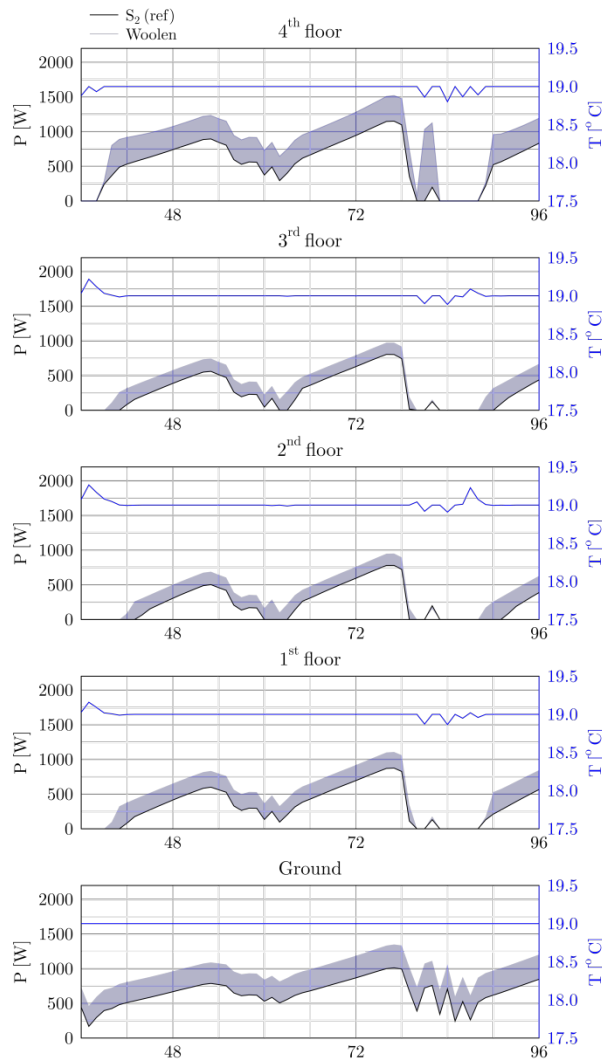| Level	Ground	1st	2nd	3rd	4th
Woolen	49.7 %	56.8 %	63 %	56.6 %	55 %
Polyurethane	18.9 %	40.6 %	57.7 %	56.4 %	55 %

Figure 15: Heating power and air temperature for the different levels (woolen insulation)

The simulation bars in blue or brown for the woollen and the polyurethane insulations are quite similar as shown in Figure 17. Simulation 2, represented by the dot is most often in the lower part of the error bar.

More specifically, the impact of the three defects will be discussed in detail hereafter. All simulations are compared to simulation S2 in Table 5.

First, we will evaluate the difference in terms of energy between simulation S1 and S2, in order to conclude on the impact of changing the thickness of the woollen insulation.

Then, we will show the difference for a change of conductivity of the woollen insulation, by quantify the energy difference between simulations S6 and S2.

Finally, we will quantify the difference between simulations S5 and S2 for a change of both thickness and conductivity (Table 5).
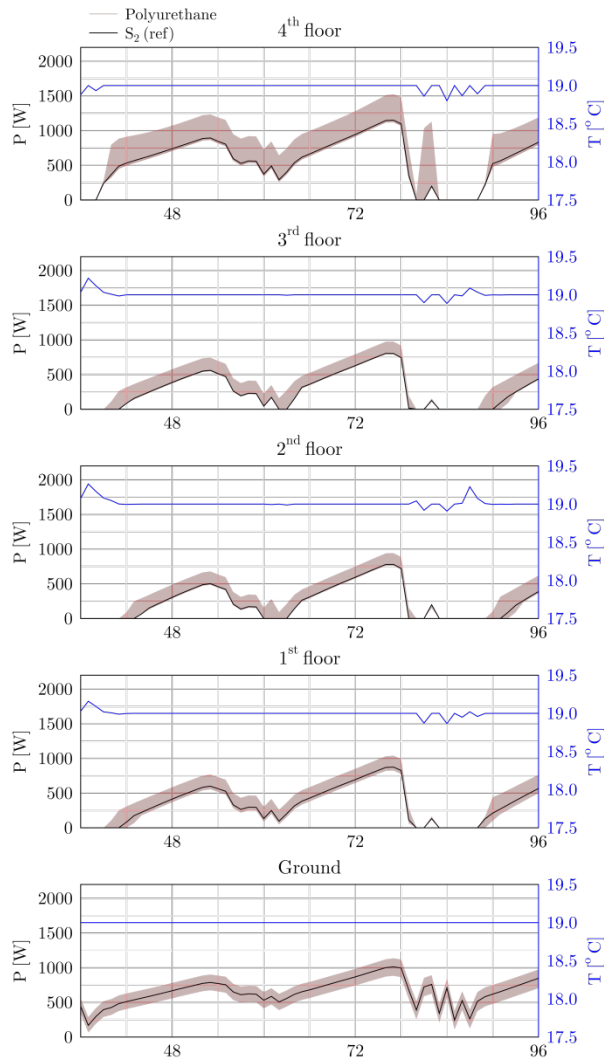

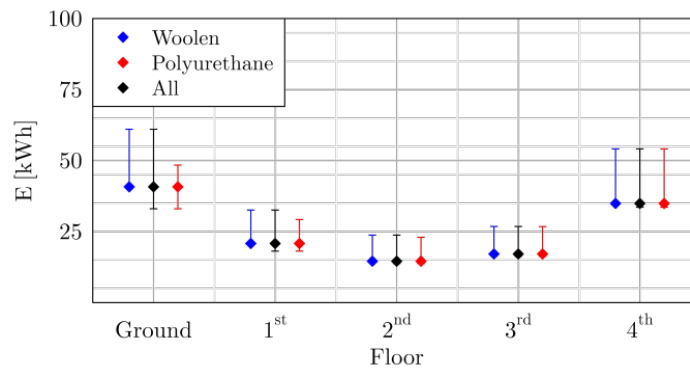*Figure 16: Heating power and air temperature for the different levels (polyurethane)*

Figure 17: Energy consumption of each floor and the variation range due to the impact of conductivity and thickness differences

Table 5: U value and energy differences normalized by the reference between each simulation and S2

Simulation	S_1	S_6	S_5	S_7	S_8	S_9	S_{10}
U [W/m²K]	58.7	67.9	74.0	59.8	49.8	71.6	60.8
Difference [%]	11.9	38.5	56	16.0	9.12	45.7	16.2

For a change in material, we focus on simulations S7 to S10 and quantify the differences between these simulations and the reference simulation (Table 5).

We can see that for this case study, the energy difference for the first defect is the lowest. A change of thickness of 3cm leads to a mean difference for the whole building of 11.9% when the U_{value} of the global envelope is of 53W/m²K for S2 and of 58.7 W/m²K for S1. The conductivity change seems to be more important than the thickness change for this case study, as mean differences of 38.5% are observed. Of course, a change of both conductivity and thickness leads to mean differences of 56.2%.

For the third defect, we supposed that polyurethane was chosen instead of woollen insulation. We see that the difference is in the range of 16 – 45.7 % depending on the thickness and conductivity value. The highest difference is observed for a thickness change, reaching 45.7%. We observe similar differences for S7 and S10. We cannot conclude here on whether the thickness impacts more than the conductivity. Moreover, it is simulation S8, which is the closest to S2, for which neither the thickness nor the conductivity is the same as S2, but the U_{value} is the closest.

The air temperature differences of the different floors are not presented here since very low differences are observed. We observed that the differences of the outside temperature surfaces between the simulations are quite low. The differences of the inside surfaces temperatures are more important, but they reach only 0.2 - 0.3 °C.

In this first application we observed, high differences among the energies when changing the conductivity, the thickness or both. Here, all simulations show important differences compared to simulation S2. These kinds of defects are a source of energy performance loss between as building's designed and as-built and would need to be corrected on site.

These defects can be located on the whole envelope or can just be part of the envelope surface. This is the reason why we have developed the new model ability to consider local material heterogeneities or defects. This will be presented in the next application.

2.2.4.4.2   Impact of a local defect or heterogeneity

With the new thermal model, we can add a local defect on the envelope and adapt the spatial discretization of the faces referring to the defect and the faces around it. The defect considered here on the southern wall is surrounded by a red square in figure 18. We have in total two defects located on the ground floor, on two different walls. The walls have the same properties than simulation S2 in Table 3. The case treated referring to the second type of defects is a lack of insulation. We consider again simulation S2 as the reference. So, the simulation with the defect is compared to simulation S2 to quantify the impact on the energy performance.
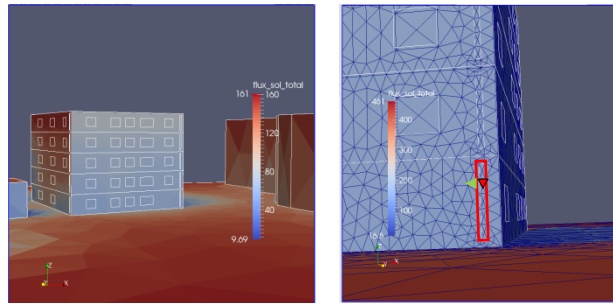
Figure 18: At the left, the studied building and at the right, a zoom on the defect of the ground floor

To add a defect in the geometry, we generated a new face (distinguished here by the white edges in the left figure 18) which is here a rectangle but can be of any shape. The defects has a size of 0.4 m² for a wall of 53 m², which represents a ratio of 0.48 % between the defects' surface and the envelope surface of the ground floor. The simulations undertaken are as before for winter conditions with a heating system. We compared the surfaces temperatures at the inside and outside of the wall for both a mesh in the defect (red line) and one located on the wall just beneath the defect (green triangle) (Figure 18). We observe a very small difference between the defect and the wall for the outside temperatures but a larger difference for the inside temperature (Figure 19); up to 2.5 °C between the mesh in the defect and a mesh just beneath. On the other hand, a maximum of 0.5°C difference is observed for the outside surface temperature (Figure 19).
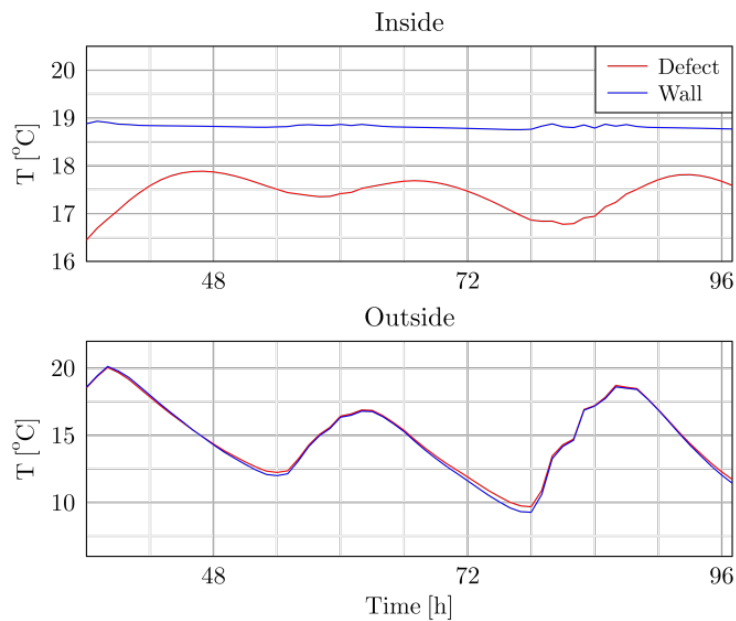

Figure 19: Single inside and outside surface temperatures of the defect and the wall
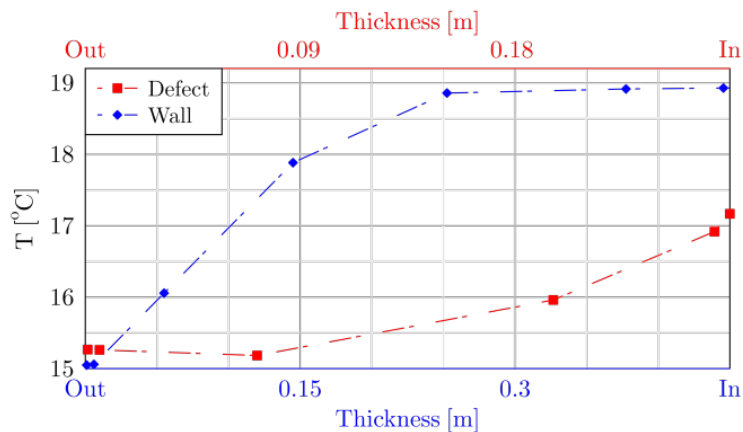
Figure 20: Temperature profile through the defect and the wall

We see on Figure 20 the temperatures for the different nodes (depths) through the wall. We observe again a very small difference for the first node, i.e. for the outside surface temperature. For the last nodes, i.e. the inside surface temperature, we observe a difference of 2 °C.

In terms of energy consumption the difference is of 2.8 %. Here, the surface ratio between the defects and the envelope walls of the ground floor is of 0.48 %. In this case study for an envelope with an exterior insulation and a local defect, we observe that the local defect can be visualized only on the inside of the building: this is important for the detection with an infrared camera.

To conclude, a building thermal model for studying defect impacts has been implemented. The defects considered in the preliminary analysis are: materials with different properties or thicknesses than the initially planned during the design stage on the entire envelope or a local defect like a lack of insulation. The model has been presented and a comparison to TrnSys showed the general coherence of the new model. First applications showed the capability of the developed model to integrate the defects under consideration. For the first type of defects located on the entire envelope, we observed that the heating power is very sensitive to both the conductivity and thickness of the chosen insulation. For the second application, when considering a local lack of insulation, for winter conditions, we observed a large impact on the inside surface temperature and a low impact on the heating power and energy, as the defect size was small.

2.3 Inverse Modelling

2.3.1 Thermal characterization of wall with quadrupole model

2.3.1.1 PRINCIPLES OF INVERSES METHOD

As previously validated (section 2.2.2), the thermal quadrupoles model can well predict the transient heat transfer in a thick wall. The inverse method, based on this numerical model, is applied here in order to make optimization of thermal properties for each layer of wall. The inverse method flow chart is shown in Figure 21. Levenberg-Marquardt algorithm (Maquart 1963) (Mathworks 2017) is used for the optimization of the unknown array U. As described in deliverable D2.3, a four-layer wall was detected experimentally. The objective wall is constructed with a mortar layer, a cinder block layer, an insulation layer and a plaster layer.
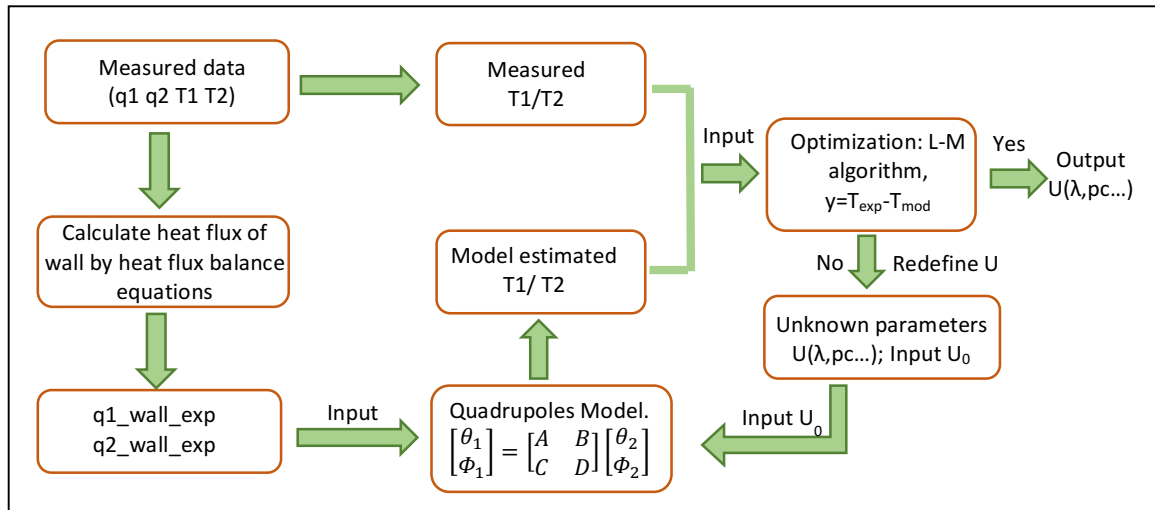
Figure 21: Inverse method to identify U

2.3.1.2 SENSITIVITY ANALYSIS

2.3.1.2.1 Local sensitivity analysis

The sensitivity is: $S_i(t) = X_i \dfrac{\partial y_k(t)}{\partial Xi}$

The numerical approximation of the sensitivity is: $S_i(t) = X_i \dfrac{\Delta y_k(t)}{\Delta Xi}$

$$S_i(t) = X_i \frac{[Y(X_1, X_2, \ldots X_{i+\Delta i}, \ldots X_k) - Y(X_1, X_2, \ldots X_i, \ldots X_k)]}{\Delta Xi}$$

(Eq. 2.26)

2.3.1.2.2 Sensitivity of front face temperature - heating face (T1)

For a square wave heating of period 24 hours, the sensitivities of 8 parameters on front face temperature T1 is calculated by local method and global Morris method, shown in Figure 22.
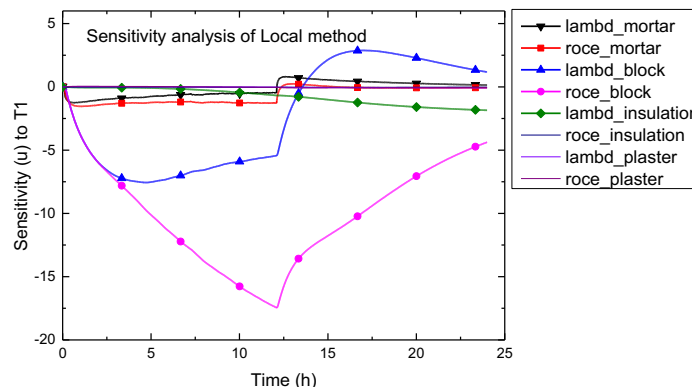
Figure 22: Sensitivity of thermal properties on front face temperature T1 (where 'lambd' represents the thermal conductivity, 'roce' represents the heat capacity)

As Figure 22 shows, the thermal capacity and thermal conductivity of cinder block is obviously sensitive to front face temperature T1 all the time, and the capacity and conductivity of mortar is lightly sensitive. The sensitivity of conductivity of insulation begins to be obvious after 12 hours. Considering these

sensitivity values and characterization time, the input unknown array U is set: U (λ_{mortar}, ρc_{mortar}, λ_{block}, ρc_{block}), the characterization time is between 1-5 hours.

2.3.1.2.3 Sensitivity of rear face temperature (T2)

For a square heating signal of period 24h, the sensitivities of 8 parameters of wall for the rear face temperature T2 is calculated by Morris method and shown in Figure 23. 4 parameters effect obviously the rear face temperature, the parameters array can be set as U (λ_{block}, ρc_{block}, $\lambda_{insulation}$, $\rho c_{plaster}$).
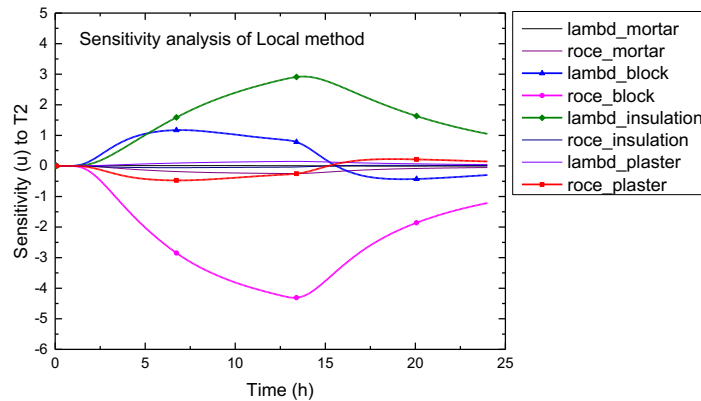
Figure 23: Sensitivity of thermal properties on the rear face temperature T2

2.3.1.3 RESULTS

Based on the sensitivity analysis, 6 thermal parameters were optimized by inverse method with the measured heat flux and temperature of wall (described in Deliverable D2.3). The optimum values of thermal parameters are listed in Table 5.

Table 5: Optimum results of thermal parameters

	λ_{mortar} (W/mK)	ρc_{mortar} (10^6 J/m³K)	λ_{block} (W/mK)	ρc_{block} (10^6 J/m³K)	$\lambda_{insulation}$ (W/mK)	$\rho c_{plaster}$ (10^6 J/m³K)
Test 1	1.17	2.36	0.84	0.92	0.045	0.53
Test 2	1.70	2.27	0.86	1.02	0.051	0.64
Test 3	1.45	2.45	0.84	0.99	0.056	0.69
Test 4	1.47	2.64	0.80	0.99	0.046	0.69
Advantage values	1.45	2.43	0.83	0.98	0.050	0.64
Reference values	1.15	1.70	0.87	0.90	0.038	0.90

In test 1, the optimum values of parameters and heat flux of front face of wall (q_1) are input to the direct modeling system, the updated output temperature is compared with the measured temperature (T_1, T_2), shown in Figure 24.

(a)   (b)

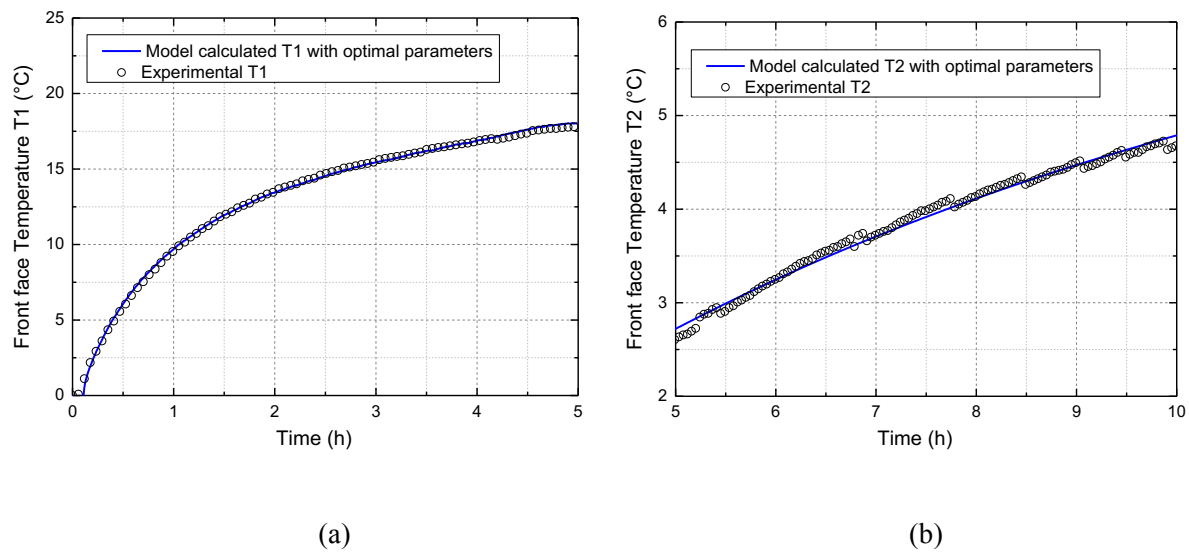*Figure 24: Comparison between measured temperature and temperature that estimated by thermal quadrupole model with the optimal results. (a) Temperature of front face; (b) Temperature of rear face.*

2.3.2   Thermal characterization of wall with finite difference

2.3.2.1   AIM:

In this section, the second part of the numerical work developed in UB is exposed. As showed in Section 2.2.3 (where the numerical part: direct heat transfer model, is discussed and validated), the aim of UB methods is to develop simultaneous experimental and numerical studies to be finally applied to characterise the wall. The experimental work is discussed in deliverables D.2.3 and D.7.2. In the following section, we present and discuss the inverse heat transfer model which is also validated. It can be defined as an optimization problem. The aim is to apply the current developed method for thermal characterisation of building materials.

2.3.2.2   BASICS OF OPTIMIZATION:

The inverse heat transfer model seeks to find a minimization solution of a mathematical problem applied to heat transfer. Thus, optimization is the method to find the best parameters values for a minimum value of a defined objective function. Bases of the mathematical formulation of the problem can be written (Rao 2009):

Suppose a function or objective function: $f : \mathbb{R}^n \longrightarrow \mathbb{R}$

Find parameter *x** minimizing the objective function: find *x*= argmin$_x$ {f(x)}*.

This is the unconstrained formulation. If some additional conditions are known the problem becomes constrained such that:

G(x)≤ 0 and *L(x) = 0*

Where: *G* and *L* are functions dependent on *x*.

In this case x^* is said global minimizer. Now, if the arguments are limited in a defined region: δ inside $\mathbb{R}^n$ so x^* becomes a local minimizer, such that:

$f(x^*) \leq f(x)$ for $\| x - x^* \| < \delta$.

These few notions about optimization are important because finding a local or a global minimizer can lead to "wrong" or "correct" optimization issues. For more information about optimization refer to (Derbal 2014) and (Bierlaire 2013).

2.3.2.3   OPTIMIZATION METHOD:

Different methods exist and can be applied to solve the actual problem: Analytical, Linear (e.g. Simplex), Non-Linear (e.g. Levenberg-Marquardt) and Heuristic (e.g. Genetic algorithm). Based on our previous studies in this context, the Levenberg-Marquadt Algorithm (LMA) is chosen to be applied in the current work.

The LMA is an optimization algorithm for parametric functions. It provides a numerical solution to the problem of function minimization, usually non-linear and depending on a set of different variables. In this work it is used to minimize the objective function described below by to identifying the optimal parameter set of the numerical model. The end of the calculation is determined by the stop criteria of the algorithm. The LMA is at the junction between the Gradient descent method and the Gauss Newton method. This algorithm is numerically programmable with Matlab software. For more details on the design of LMA programming stages, please refer to (Kenneth 1944) (Maquart 1963) (Mathworks 2017). In this work, we do not provide more details on the mathematical formulation nor on its encoding but the algorithm steps are presented after this paragraph. Moreover, one must keep in mind that direct heat transfer is a well-posed problem where one can simulates temperature for known parameters (please refer to section 2.2.1) and inverse heat transfer is an ill-posed problem where one knows the temperatures and try to find some parameters. The parameters in our study case are the thermo-physical properties in the heat equation (Eq. 2.1).

The LMA is a descent method that uses both operators: Jacobian and Hessian. Elements of the derivative used in the calculation are the sensitive parameters on which depends the choice of the descent direction and the damping factor. Hereafter the algorithm is explained step by step (refer to literature):

1. Choose initial parameter values and an initial damping factor (λ_A generally equals to 10^4); iteration 1 starts (i=1).

2. Calculate the Jacobian (Iteration i).

3. Check the current parameter (p_i) optimality (all sensitive elements are lower than a user defined value): Y/N = stop/continue.

4. Find new parameter $p_{i+1} = p_i + h_{LMA}$ (here, h_{LMA} is the descent direction).

5. Compare $F(p_{i+1})$ to $F(p_i)$ and then calculate the new damping factor. If $F(p_{i+1}) - F(p_i) < 0$ then choose a lower λ_A and go to step 2 else choose a higher λ_A and go to step 4.

Here, F is the objective function and p_i the parameters to be estimated as defined in next section showing also a detailed diagram of LMA for the estimation of thermo-physical properties.

To discuss the method, we suppose a multilayer to be studied as shown on Figure 25. The method applied here, can be extended to other study cases and multilayer taking into account the general hypothesis (discussed also in section 2.2.1). The parameters to be evaluated are the middle layer thermal conductivity λ (W/mK) and its volumetric heat capacity ρC (J/K.m^3). The input data for the LMA are the measured temperatures, the simulated temperatures based on the finite differences method and the initial parameters (λ_0, ρC_0). The iterative algorithm fits the simulated temperatures to the measured temperatures with the nonlinear least squares method. The process is stopped whenever one of the 3 stopping criteria below is verified. Fitting the curves means minimizing the objective function defined hereafter.
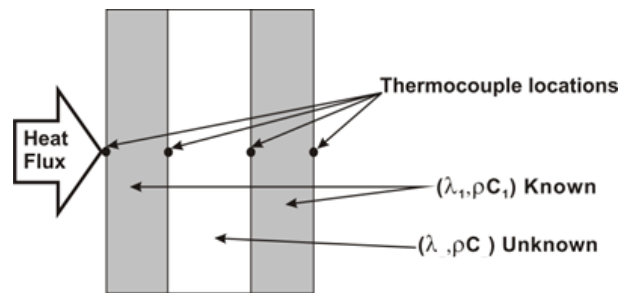
Figure 25: Example of studied sample

Firstly, a matrix is designed based on the normalized differences. The values of this matrix elements indicated here as $f_{i,j}$ are equal to the weighted difference between the simulated temperatures T_{sim} and the measured temperatures T_{meas} at each iteration $i = 1, ..., N$ and to the interfaces $j = 1, 2$ (Eq. 2.27) and (Eq. 2.28).

$$f_{i,j}(\boldsymbol{p}) = \frac{T_{meas}(i,j) - T_{sim}(i,j,\boldsymbol{p})}{\max(\boldsymbol{T_{meas}}) - \min(\boldsymbol{T_{meas}})}$$

(Eq. 2.27)

Where: $\boldsymbol{p}$ is the vector of the parameters to be defined (λ and ρC).

The objective function is defined as follows:

$$\boldsymbol{F}(\boldsymbol{p}) = \sum_{i,j} \left(f_{i,j}(\boldsymbol{p}) \right)^2$$

(Eq. 2.28)

At every iteration, a new set of parameters is being tested and a new value for the objective function is computed. On Figure 26 the diagram illustrates the algorithm flowchart. It also indicates under which circumstances the optimization stops:

- The objective function reaches a value less than ε, the threshold defined in the algorithm.

- The difference between two successive sets of parameters is less than an established minimal variation expressed as Δp_{min}.

- The maximum number of iteration k_{max} is reached.

Once the optimization is complete, an estimated set of parameters is thus obtained. The quality of fit is graphically appreciated through the comparative display of both measured and simulated temperatures. The residual differences allow for the calculation of standard deviations in order to quantify the fit.
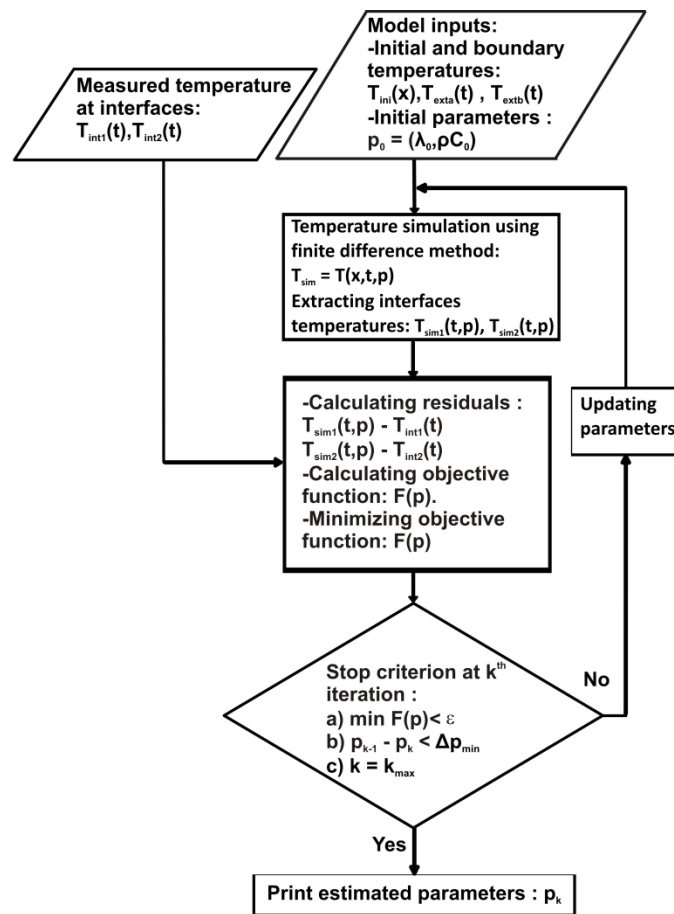
Figure 26: Parametric estimation by inverse method diagram.

2.3.2.5 MODEL VALIDATION: INVERSE METHOD VS STANDARD TEST:

Now, we consider the unknown layer on Figure 25 to be known: commercially available PVC. The two other layers are made of the same material to have a 3-layer sample of PVC to be tested. The chosen material to validate the inverse method is homogeneous and inert. Its properties do not vary with time and it is well known material.

The symmetrical heat flow meter method of one PVC test sample in a sandwich configuration as described in the ISO 8301:1991 standard has been set up (Derbal 2014). The accuracy of the method is about 5% and the reference values are in Table 6.

Table 6: Reference values of thermophysical properties for the tested PVC

Material	λ(W/K.m)	ρC (J/K.m^3)
PVC	$1.80 \cdot 10^{-1}$	$1.46 \cdot 10^{6}$

Next the reference values are compared to those obtained by the inverse method applied to the 3-layer sample of PVC.

To do this, test temperatures were recorded by thermocouples (Figure 27) placed on the multilayer as shown on Figure 25. The obtained data are then used to perform calculation following the flowchart of Figure 26. The results are shown hereafter.
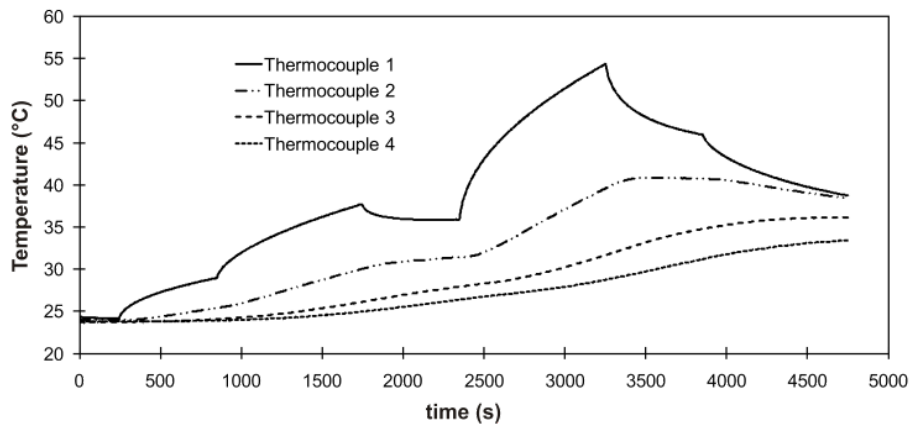
Figure 27: Time series of recorded temperatures during a test

At the two interfaces (Figure 25) the simulated temperatures by the current inverse method are fitted to the measured temperatures during the optimization process (Figure 28 and Figure 29)

We observe a very good agreement between the measured temperatures and the simulated temperatures after optimization by the weighted non linear least squares method. The results obtained with this method allow us to conclude that the maximum difference between the curves is of 0.2°C and that the standard deviations are respectively $\sigma_1 = 0.099$°C and $\sigma_2 = 0.068$°C for the first and for the second interfaces. For the test number 1, the obtained thermal conductivity and volumetric heat capacity values are: $\lambda_{cal} = 1.76 \cdot 10^{-1}$ W/K.m, $\rho C_{cal} = 147.14 \cdot 10^{4}$ J/K.m^3 with relative errors of 2.82% and 0.77% respectively. Using the same set up (Figure 25), 14 tests were carried out. The results are presented in Table 7.

Figure 28: PVC multilayer results: simulated and measured temperature at the first interface.

Figure 29: PVC multilayer results: simulated and measured temperature at the second interface.

Table 7: Simulation results for the PVC multilayer series of tests

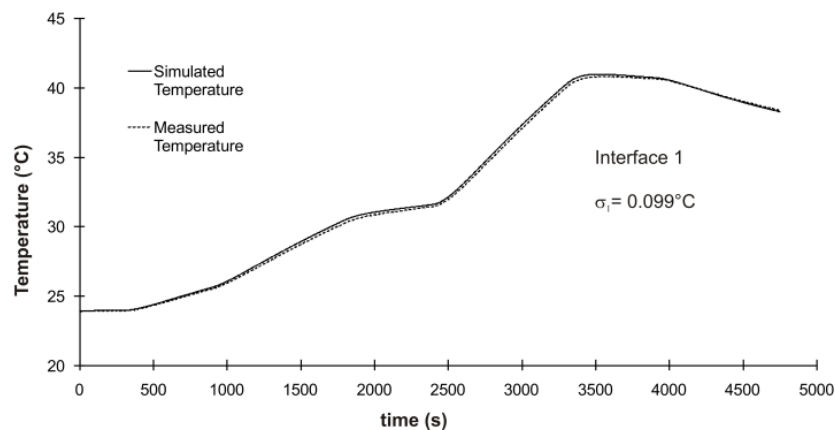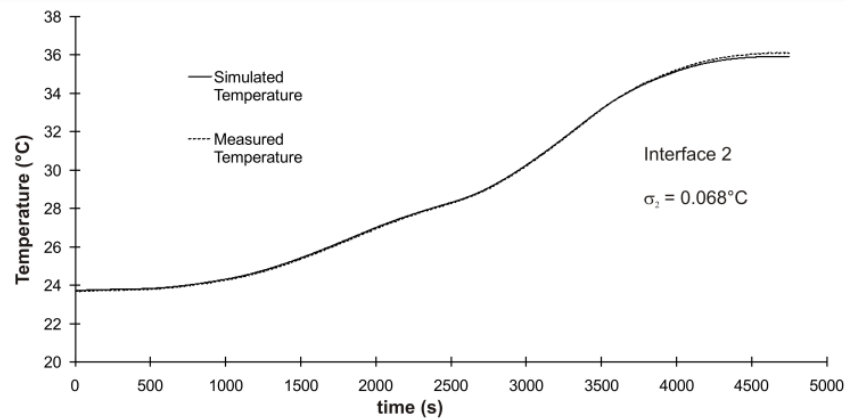| test number	λ_{cal}			ρC_{cal}		
	value $(10^{-1}$ W/K/m)	absolute error $(10^{-2}$ W/K/m)	Relative error (%)	value $(10^4$ J/K/m^3)	absolute error $(10^3$ J/K/m^3)	Relative error (%)
1	1,76	0,51	2,82	147,14	11,25	0,77
2	1,81	0,03	0,17	146,51	4,88	0,33
3	1,83	0,13	0,72	146,52	5,00	0,34
4	1,81	0,00	0,01	146,47	4,54	0,31
5	1,81	0,00	0,01	146,52	5,00	0,34
6	1,81	0,00	0,00	146,52	5,00	0,34
7	1,81	0,01	0,05	146,30	2,85	0,20
8	1,81	0,02	0,09	145,92	0,96	0,07
9	1,81	0,00	0,00	146,02	0,00	0,00
10	1,81	0,00	0,00	146,02	0,03	0,00
11	1,82	0,02	0,09	145,93	0,83	0,06
12	1,81	0,00	0,02	145,98	0,36	0,02
13	1,82	0,02	0,13	146,10	0,78	0,05
14	1,82	0,02	0,13	145,80	2,21	0,15
mean values	1,81	0,06	0,30	146,27	3,12	0,21

Reading the results (Table 7) of the estimated parameters makes it possible to assess the accuracy and the repeatability of the method. The estimation errors obtained are low (<5%) and stem partly from the numerical model and partly from measurement noise. Indeed, an uncertainty in the measured temperatures (boundary conditions and initial condition) necessarily leads to a deviation during the simulation. The errors generated by the numerical model are added to these uncertainties.

2.4   Conclusion

In the first section, a direct wall model is presented in detail based on the finite difference method. This model is applied for both direct modelling and inverse modelling. The direct detailed modelling is a thermal envelope model for studying defects impacts. It is a model where the spatial discretization can be adapted to the size and localization of the defect. In this context, a new model was developed and

validated. The defects considered in the preliminary analysis are: materials with different properties or thicknesses than the initially planned during the design stage on the entire envelope or a local defect like a lack of insulation. The model has been presented and a comparison to TrnSys showed the general coherence of the model. First applications showed the capability of the model to integrate the defects we wanted to consider. For the first type of defects located on the entire envelope, we observed that the heating power is very sensitive to both the conductivity and thickness of the chosen insulation. For the second application, when considering a local insulation lack, we observed for winter conditions, a high impact on the inside surface temperature and a low impact on the heating power and energy, as the defect's size was small.

With the inverse modelling, temperatures and heat fluxes are measured and, using two methods of thermal wall modelling (quadrupole model and finite differences model) and an optimization algorithm the U values are obtained. The estimation errors obtained by the finite difference model and the LMA optimisation method are lower than 5%. The results show that the developed inverse model is able to estimate thermophysical properties of a multilayered tested sample. This corresponds to the general case of a wall composition in buildings. Thus, we expect that the method based on the finite difference model and the LMA optimisation method can be applied to other test configurations in the framework of Built2Spec project.

3 3D automated referencing

3.1 Introduction

3.1.1 Problem position

The goal of the 3D automated referencing task in the context of the B2S project is to be able to align a set of 2D thermal images from a building (or buildings) onto a 3D model (or models) of the same building in order to visualize its thermal quality. The 3D model is extracted from the BIM files of the building(s) while thermal images are captured on site with special equipment (thermal cameras).
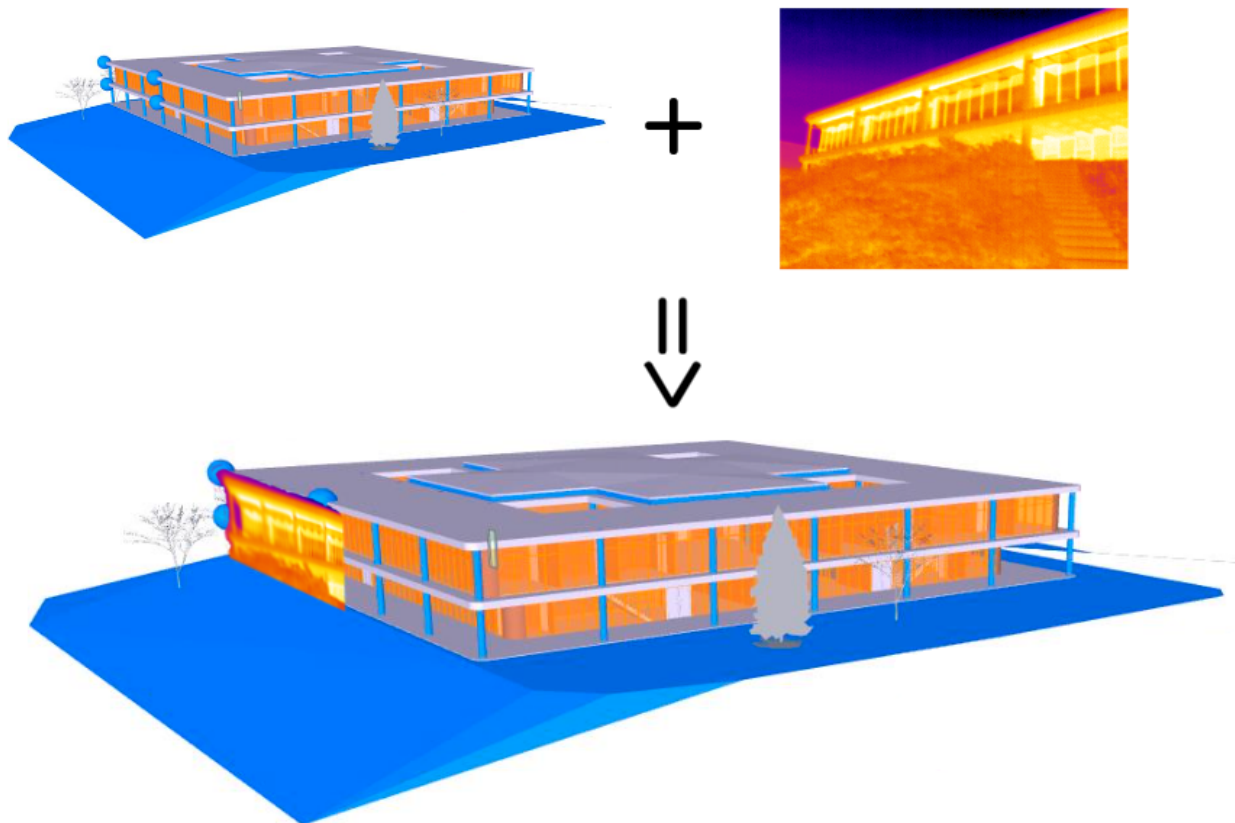
Figure 30: Illustration of the 3D automated referencing task performed here manually for illustration purpose.

The ideal process is illustrated in Figure 30 where the process had been performed **manually**. This task is particularly challenging since the image may contain only a very limited part of the 3D model. Basically, there are two hard problems to be tackled here:

- Finding automatically some corresponding points in the thermal image and in the 3D model;
- Performing an automated matching between those points.

Those tasks are especially hard and prove to be, as of now, a true challenge since to the best of our knowledge this has never been achieved before. Finding the correspondences and doing the matching can be done manually but the automated way remains a scientific lock.

3.1.2   3D Registration aim

The task to be achieved can be related to Augmented Reality (AR) where some virtual objects have to be displayed on top of images (or videos) of the real world in a plausible way. The plausible integration actually means that the virtual objects have to be positioned, oriented and scaled so that they can be displayed as if they were part of the real world. These correct orientation, position and scaling is generally referred to as the 3D registration problem (Azuma 1997).

In this Section, we first detail how to achieve this 3D registration problem in the context of the B2S project. 3D registration aligns the virtual and the real environments so that virtual objects can be merged into the real world at their desired positions and orientations. When the real environment is known, the registration problem is reduced to a localization problem in 3D namely determining the viewer's pose (i.e. position and orientation) in the real environment coordinate system. Depending on the devices used, localization can be mainly divided into five categories (Yang 2016) (Billinghurst, Clark et Lee 2015):

1. Magnetic-based localization relies on the properties of magnetic fields to calculate the pose of the receiver, which is attached to the viewer.
2. Vision-based localization uses information retrieved from images captured by cameras to find the pose of the viewer. Different kinds of cameras may be used, e.g. traditional RGB cameras, depth cameras, etc.
3. Inertial-based localization uses Inertial Measurement Unit (IMU), which usually includes accelerometers, gyroscopes and magnetometers. It measures translational movements, the orientation relative to gravity and the velocity of the viewer.
4. GPS-based localization relies on satellite navigation to roughly estimate the viewer's geographical location.
5. Hybrid localization combines the advantages of the above-mentioned approaches in order to give a robust and precise estimation.

Magnetic-based approaches need special preparation on target objects, which increases the workload. Inertial-based and GPS-based approaches can only give a rough estimation of the viewer's position, which usually cannot satisfy the precision requirements of AR systems, which is the precision we aim for this task. The vision-based approach has the advantage to be simple and cheap, i.e. using images captured by cameras to estimate the position of cameras with respect to the world. This method is also similar to the humans' visual perception. For these reasons, vision-based localization gets the most attention in the AR community and is the method we focus on for this task.

Most of the time, 3D registration boils down to estimating the location of the viewer (i.e. the camera) since the viewer moves with respect to the environment. It consists of estimating the 3D position and 3D orientation of the camera (also known as pose or extrinsic matrix $[\mathbf{R}|t]$, for more details see Section 3.2.1) for each frame captured by the camera. If the viewer's pose in the previous frame is known, it can be used as additional information for estimating the pose of the current frame. The usage of the previous pose to estimate current pose is called *narrow baseline tracking*. For the first frame of the input video sequence, or if the pose of previous frame is not found (i.e. tracking failure), the viewer's pose can only be estimated from information in the current frame. In such a case, it is called *wide baseline localization*. In this task, we will focus only in wide baseline localization techniques since we do not have any prior information concerning the localization of the viewer (and the camera) with respect to buildings.

3.2 Camera pose calculation

In this project, we need to know where each image was taken to be able to register it with respect to a building 3D model extracted from a BIM file. Knowing the camera 3D position and 3D orientation in a specific frame linked to, in our case, a building is called in computer vision "camera pose computation". In the remainder of this section, we first recall some basic notions of computer vision before explaining how the camera pose can be computed from correspondences between points in the 3D model and the same points in a 2D image.

3.2.1 Pinhole camera model

The camera maps the 3D world onto a 2D image. One of the simplest camera model used to do this mapping is the pinhole camera model. This model is extensively detailed in (Hartley et Zisserman 2003).

The basic pinhole camera uses a central projection of points onto a plane (cf. Figure 31).
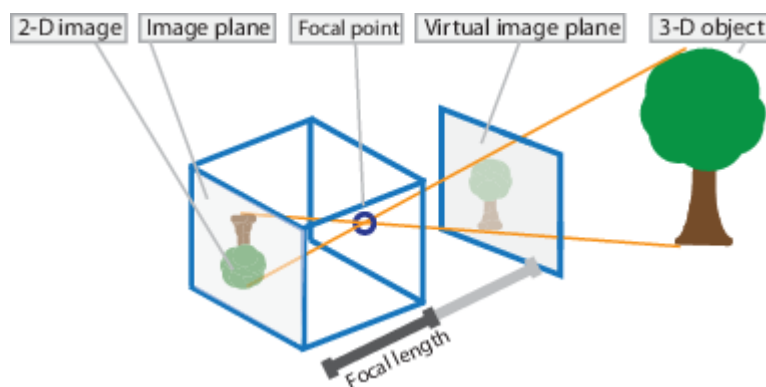
Figure 31: Pinhole camera model. Source MathWorks[4].

The centre of projection, also called principal point, (O_c in Figure 32) is considered as the origin of a Euclidian coordinate system linked to the camera. The plane parallel to the axes X_c and Y_c and at coordinate $+f$ on the Z_c axis is called the virtual image plane, or image plane in short, (Figure 32) where f is the focal length of the camera. The axis along Z_c going through O_c is called the principal axis.
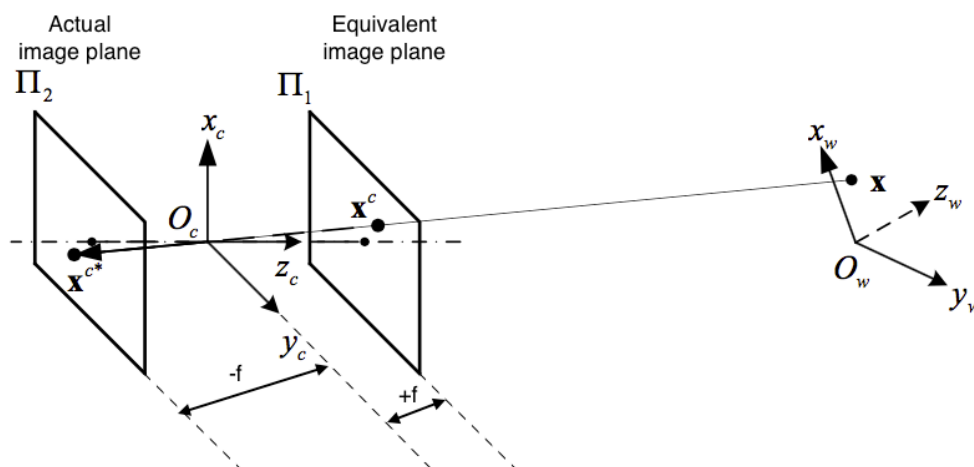
Figure 32: Geometry of a pinhole camera and associated frames, from (Yang 2016).

---

[4]https://fr.mathworks.com/help/vision/ug/camera-calibration.html

Using this camera model, where O_w represents the center of the coordinate system of the real environment, and assuming that the pinhole camera model has no distortion (see Section 3.2.2.2); light coming from a world point X goes through the camera's optical center O_c and forms an image X^{c*} on the camera's actual image plane. For the sake of simplicity, the image point X^c on the camera's equivalent image plane is often used instead.

Using this model, a point in space $X = (X, Y, Z)_c^T$ in the camera frame is mapped to the point $x = (fX/Z, fY/Z, f)_c^T$ on the image plane. The different coordinates subscripts indicate the associated frames. As explained in (Hartley et Zisserman 2003), this correspondence can be expressed in *homogeneous coordinates* as:

$$\begin{pmatrix} X \\ Y \\ Z \\ 1 \end{pmatrix}_c \rightarrow \begin{pmatrix} fX \\ fY \\ f \end{pmatrix}_c = \begin{bmatrix} f & & & 0 \\ & f & & 0 \\ & & 1 & 0 \end{bmatrix} \begin{pmatrix} X \\ Y \\ Z \\ 1 \end{pmatrix}_c$$

(Eq. 3.3.1)

Homogeneous coordinates are a system of coordinates used in projective geometry that allows defining a point at infinity (when the last coordinate is equal to 0).

To project a 3D point from a world frame to a 2D point in an image, we need to determine how to relate the different coordinate frames depicted in (Figure 32), the world frame (attached to the house in our case), the camera frame (located in O_c) and the image frame. This leads to the definition of intrinsic and extrinsic camera parameters. The overall process is summarized in Figure 33 and explained in the following.
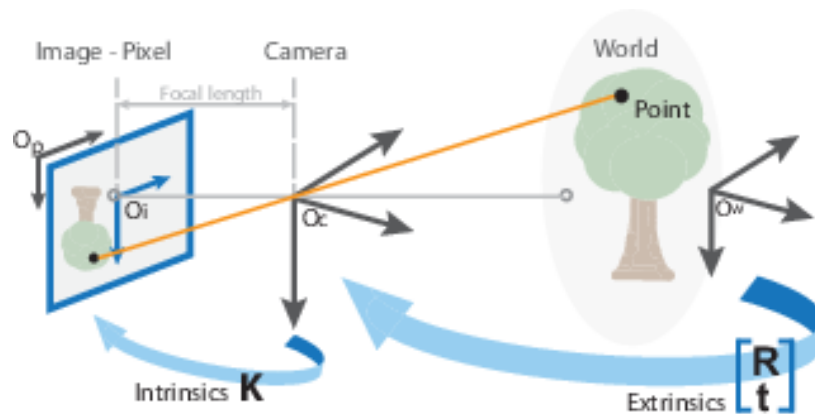

Figure 33: Transformation applied to a 3D point in World space coordinates projected onto the 2D image plane. Source MathWorks[5].

3.2.2 Intrinsic camera parameters

The intrinsic camera parameters are the parameters required to use a pinhole model for a camera. It is generally admitted that there are 5 intrinsic parameters and their usual representation is a matrix called **K**,

---

see (Eq. 3.3.3). In the following, we first present the classical camera pinhole model before detailing how the intrinsic parameters are computed.

3.2.2.1 LINEAR PINHOLE CAMERA CALIBRATION MATRIX

The origin of the image frame is usually not located at the principal point p. If $(p_x, p_y)^T$ are the coordinates of the principal point p in the image frame, (Eq. 3.3.1) is transformed into:

$$\begin{pmatrix} X \\ Y \\ Z \\ 1 \end{pmatrix}_c \rightarrow \begin{pmatrix} fX + Zp_x \\ fY + Zp_y \\ f \end{pmatrix}_c = \begin{bmatrix} f & & p_x & 0 \\ & f & p_y & 0 \\ & & 1 & 0 \end{bmatrix} \begin{pmatrix} X \\ Y \\ Z \\ 1 \end{pmatrix}_c = K[I \quad | 0] \begin{pmatrix} X \\ Y \\ Z \\ 1 \end{pmatrix}_c$$

(Eq. 3.3.2)

In (Eq. 3.3.2), K is called the camera intrinsic matrix. The pinhole camera model presented previously assumes that the pixels in the image are squares, but it is not always the case. Coordinates in the image frame are often expressed in pixels. The number of pixels per unit distance in image coordinates is m_x (resp. m_y) in the X (resp. the Y) directions. The two X and Y directions may not be exactly orthogonal and a skew coefficient s is added to the calibration matrix:

$$K = \begin{bmatrix} \alpha_x & s & x_0 \\ & \alpha_y & y_0 \\ & & 1 \end{bmatrix}$$

(Eq. 3.3.3)

where $\alpha_x = fm_x$, $\alpha_y = fm_y$ and $(x_0, y_0)^T_{Img}$ are the coordinates of the principal point in pixel dimensions with $x_0 = m_x p_x$ and $y_0 = m_y p_y$.

3.2.2.2 RADIAL AND TANGENTIAL DISTORTIONS

The above equation stands for a pinhole camera and supposes a linear model of the imaging process. That might not be the case for real lenses. The most important deviation is generally a radial distortion due to the lens (Figure 34) but a tangential distortion may also occur if the lens and the sensor are not parallel.
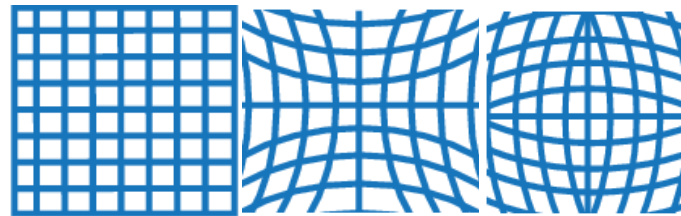
3.2.2.2.1 Radial distortion

Figure 34: No distortion (left) and radial distortion illustration with (middle) negative radial distortion – pincushion and (right) positive radial distortion – barrel. Source MathWorks[6].

---

[6]https://fr.mathworks.com/help/vision/ug/camera-calibration.html

To correct these distortions, we need to transform the image as if it had been obtained under a perfect linear transformation. The radial distortion is modelled as a distortion factor $L(r)$, which is a function of r, the lens radius.

The distorted points are denoted as $(x_{corrected}, y_{corrected})$:

$$x_{corrected} = L(r)x$$
$$y_{corrected} = L(r)y$$

(Eq. 3.3.4)

where (x, y) are the undistorted pixel locations. The x and y coordinates are in normalized image coordinates. Normalized image coordinates are calculated from pixel coordinates by translating to the centre of radial distortion and dividing by the focal length in pixels. We also have $r^2 = x^2 + y^2$.

Barrel and pincushion distortions (Figure 34) are quadratic, meaning they increase as the square of distance from the centre. The $L(r)$ function is modeled as:

$$L(r) = 1 + \kappa_1 r^2 + \kappa_2 r^4 + \kappa_3 r^6$$

(Eq. 3.3.5)

Typically, two coefficients are sufficient for calibration. $\{\kappa_1, \kappa_2, \kappa_3, x_c, y_c\}$ are the coefficients for radial correction and are considered are a part of interior camera calibration, with (x_c, y_c) being the center of radial distortion used to normalize the coordinates. The camera principal point is often used as (x_c, y_c) and as a consequence only $\{\kappa_1, \kappa_2, \kappa_3\}$ need to be determined.

3.2.2.2.2 Tangential distortion

Tangential distortion occurs because the lenses of the camera might not be perfectly parallel to the imaging plane (Figure 35). It can be corrected via the formulas:

$$x_{corrected} = x + [2p_1 xy + p_2(r^2 + 2x^2)]$$
$$y_{corrected} = y + [p_1(r^2 + 2y^2) + 2p_2 xy]$$

(Eq. 3.3.6)

where p_1 and p_2 are the tangential distortion coefficients of the lens.

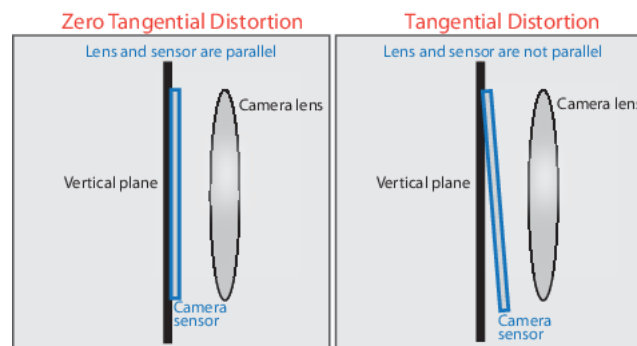*Figure 35: Tangential distortion illustration. Source MathWorks[7].*

---

[7]https://fr.mathworks.com/help/vision/ug/camera-calibration.html

In order to compensate for the distortions presented above, a calibration procedure is generally carried out which allows for computing the distortion coefficients $\{\kappa_1, \kappa_2, \kappa_3, p_1, p_2\}$. There are several ways to perform such a calibration by using a planar target (more details in Section 3.2.4) or using a special 3D target, for more details the reader is referred to (Hartley et Zisserman 2003) or (Zhang 2000).

3.2.3 Extrinsic camera parameter

The extrinsic camera parameters express the rotation and translation transformations from the world coordinates frame to the camera coordinates frame. A point $\boldsymbol{X_C}$ represented in non-homogeneous coordinates in the world frame by $(x_1, x_2, x_3)_W^T$ would be expressed in the camera coordinate frame as:

$$\begin{pmatrix} x_1 \\ x_2 \\ x_3 \end{pmatrix}_c = R \begin{pmatrix} x_1 \\ x_2 - C \\ x_3 \end{pmatrix}_w$$

(Eq. 3.7)

where C is the coordinate of the camera center (O) in the world coordinate frame and R is a $3x3$ rotation matrix representing the orientation of the camera coordinate frame. The (Eq. 3.7) expressed in homogeneous coordinate would give:

$$\begin{pmatrix} x_1 \\ x_2 \\ x_3 \\ 1 \end{pmatrix}_c = \begin{bmatrix} R & -RC \\ 0 & 1 \end{bmatrix} \begin{pmatrix} x_1 \\ x_2 \\ x_3 \\ 1 \end{pmatrix}_w$$

(Eq. 3.8)

As a consequence, (Eq. 3.8) can be written as:

$$\boldsymbol{X_c} = [R \quad |t] \boldsymbol{X_w}$$

(Eq. 3.9)

with $t = -RC$ and $[R|t]$ represent the extrinsic parameters of the camera.

3.2.4 Camera geometric calibration and pose calculation

Putting (Eq. 3.3.3) and (Eq. 3.9) together leads to:

$$\begin{pmatrix} u \\ v \\ 1 \end{pmatrix}_{Im} \propto K[R|t] \begin{pmatrix} x_1 \\ x_2 \\ x_3 \\ 1 \end{pmatrix}_w$$

(Eq. 3.10)

With $(u, v, 1)^T$ the coordinates in pixels on the image. This relation is defined with respect to a scale factor.

Calibrating a camera and calculating its pose boils down to estimating all the 11 parameters (or 10 if $s = 0$) of $P = K[R|t]$:

$$P = \begin{bmatrix} \alpha_x & s & x_0 \\ 0 & \alpha_y & y_0 \\ 0 & 0 & 1 \end{bmatrix} \begin{bmatrix} & & & t_x \\ & R_{3x3} & & t_y \\ & & & t_z \\ 0 & 0 & 0 & 1 \end{bmatrix}$$

(Eq. 3.11)

These 11 parameters are $\alpha_x, \alpha_y, s, x_0, y_0$, (the *intrinsic* parameters), the 3 rotation angles and the 3 translation (*extrinsic*) parameters. Those parameters are usually computed separately in a calibration phase (*intrinsic* parameters) and a pose computation phase (*extrinsic* parameters). The calibration phase usually needs to be performed only once per camera while the pose computation is performed at run-time.

Various methods have been proposed to calculate the intrinsic and extrinsic parameters for a specific camera. Note that the camera is supposed to keep the same focal length f during the whole process. This is usually done using multiple different views of a known pattern as for example a checkerboard pattern (Figure 36).
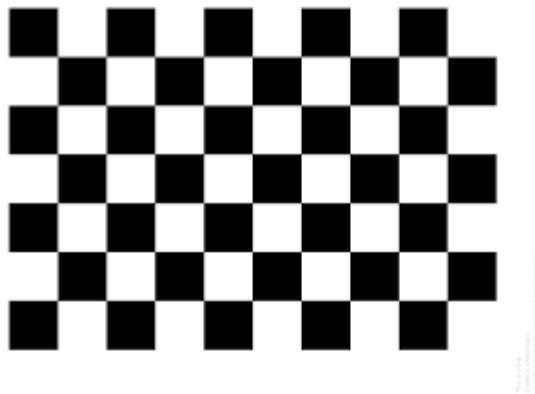
Figure 36: Checkerboard pattern used for camera calibration.

There are different methods to calculate these parameters, for example the Direct Linear Transform (DLT) method (Abdel-Aziz et Karara 1971, Awrangjeb, Lu et Fraser 2012), Zhang's method (Zhang 2000) or, Tsai's algorithm (Tsai 1987). Most calibration methods are implemented in open source computer vision libraries such as OpenCV[8].

3.3 Texture and geometric based localization

3.3.1 Introduction

We already mentioned in the introduction that in this task we focused on vision-based *wide baseline localization* methods in order to compute the solution of the 3D registration problem. The idea is to compute the extrinsic parameters from a camera recording a building, in order to superimpose on the building some thermal images. It is out of the scope of this deliverable to go into details about the numerous methods proposed to solve this problem. For more details, the interested reader is referred to a recent survey on pose estimation computation in Augmented Reality, (Marchand, Uchiyama et Spindler 2016).

Vision-based wide baseline localization techniques can be split into three main categories:

---

[8]http://opencv.org

- Fiducial marker-based localization;
- Texture-based localization;
- Geometry-based localization.

Fiducial marker-based localization techniques rely on the presence in images of fiducial markers (Figure 37). These markers are man-made artificial objects, often planar, that are placed in the field of view of the camera as reference points to simplify the pose computation. A single marker is sufficient to compute the camera pose but the size of the marker in the image needs to be quite large. Given our goal (adding information on a building), this requirement makes it impossible for us to rely on this family of techniques since we would need to attach some gigantic markers to the building we want to study. This proves impossible in practice for the Build2Spec project and this is why these techniques are not presented here. As a consequence, in the following we detail texture-based and geometry-based localization techniques.

Figure 37: Examples of fiducial markers used in Augmented Reality. From left to right: ARTag (Fiala 2005) marker, ARToolKit (Kato et Billinghurst 1999) marker, Circular Marker (Naimark et Foxlin 2002) and Random Dot Marker (Uchiyama et Saito 2011).

3.3.2 Texture based localization

Texture-based techniques usually rely on local features for wide baseline localization. These features can be interest points (Lowe 1999) or interest regions (Forssén et Lowe 2007). A high dimension textual descriptor is constructed for each local feature, and the distance between descriptors is used to measure the similarity between the corresponding local features. Then, feature correspondences can be established according to these similarities. Most of commercial Software Development Kits (SDKs), such as Metaio (bought by Apple in 2015), Vuforia (from the PTC company), provide localization tools based on this technique.

The whole procedure contains two stages. (1) Offline training stage: the features of model objects are extracted and descriptors are calculated. Then a database is created from these descriptors and the positions of features. (2) Online localization stage: for each input image, the features of scene objects are extracted and descriptors are calculated. Then these features are matched with model features stored in the database. Finally, point correspondences are established and the camera pose of the current image is estimated.

There are three basic tasks in the whole procedure above: feature extraction is dedicated to localizing visual salient features; feature description is used to construct the high dimension descriptor from the texture of the local patch around each feature; feature matching is used to establish correspondences according to descriptors.

3.3.2.1 FEATURE EXTRACTION

Interest points include geometric corners as well as the points in an image where the image intensity changes significantly. Usually, we refer to both of them as *corners* (Rosten, Porter et Drummond 2010) in a general sense. Curvature maxima can be extracted to detect geometric corners from the contours of

objects (Awrangjeb, Lu et Fraser 2012). Second-order derivatives or auto-correlation are used to extract general corners, such as Difference of Gaussian (DoG) (Lowe 1999), Harris corner detector (Harris et Stephens 1988), Shi-Tomasi detector (Shi et Tomasi 1994). SURF uses the determinant of the Hessian matrix and relies on integral images for speeding up the process of features computation (Bay, Ess, et al. 2008). Pixel intensity comparison is also used to detect corners more efficiently (FAST) (Rosten et Drummond 2006).

Thick lines and interest regions can be used as features as well. Line Segment Detector (Grompone von Gioi, et al. 2010) (LSD), Line Signature (Wang, Neumann et You 2009) or line segment matching approach from (Zhang et Koch 2013) offer some methods for line segments extraction. (Donoser et Bischof 2006) give a good method for extracting interest regions (MSER).

Regarding the wide baseline localization problem, feature repeatability is an important quality of the extraction method. A feature is said to be repeatable when the same feature is extracted from different images of the same scene, despite perspective distortions or imaging noise. A repeatability evaluation of different methods on point feature extraction can be found in (Ballesta, et al. 2008), which concludes that Harris corner detector (Harris et Stephens 1988) works best under different scales and viewpoints.

A descriptor faster than SIFT and SURF has been proposed recently: ORB (Rublee, et al. 2011). It is a very fast binary descriptor based on BRIEF (Calonder, Lepetit et Strecha, et al. 2010) which is invariant in rotation and resistant to noise.

3.3.2.2 FEATURE DESCRIPTION

SIFT, proposed by David G. Lowe (Lowe 1999), is one of the most famous feature descriptor. It is based on the computation of image gradients quantized into orientation histograms. After having extracted interest points, the 16×16 neighbourhood of each interest point is uniformly divided into 4×4 sub-regions. In each sub-region, the sum of the gradient magnitudes is calculated in 8 directions. The descriptor of the interest point is created by assembling the sums of the gradient magnitudes in the 8 directions of all the 4×4 sub-regions into a 128 dimension vector (cf. Figure 38). The vector is then normalized to achieve illumination invariance.
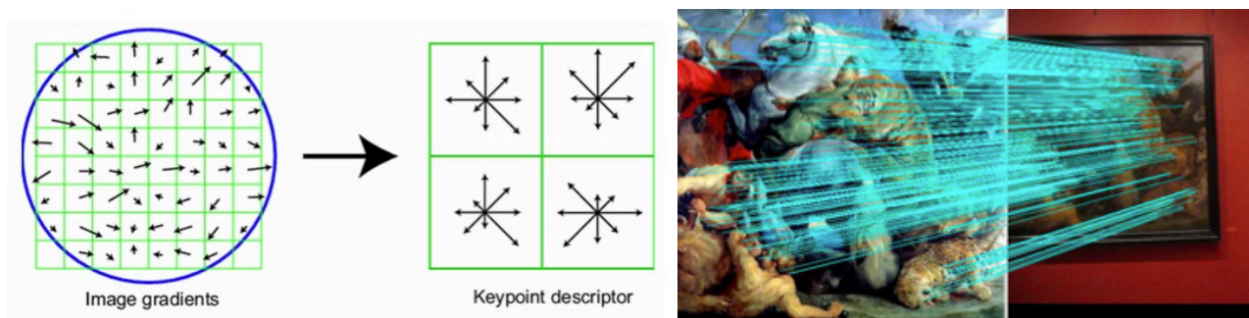
Figure 38- SIFT descriptor. Left: Image gradients of 16×16 neighbourhood of interest points and sums of the gradient magnitudes in 8 directions of 4×4 sub-regions (Lowe 1999). Right: Result of detection and matching of SIFT descriptors.

Following this idea, other kinds of descriptors were further proposed. SURF (Bay, Ess, et al. 2008) relies on the distribution of first order Haar wavelet responses in x and y directions. BRIEF (Calonder, Lepetit et Ozuysal, et al. 2012) is a binary descriptor created by comparing two sequences of pixels located near the extracted feature. These two methods are used for interest point features. For line segment features, (Bay, Ferraris et Van Gool 2005) use colour histograms as descriptors, (Wang, Wu et Hu. 2009) adopt a

SIFT-like approach to create the MSLD descriptor. (Forssén et Lowe 2007) apply SIFT to create an interest region descriptor.

3.3.2.3   FEATURE MATCHING

Since descriptors are high dimension vectors, the most common approach is to calculate a distance between different vectors, such as the Euclidean distance (Lowe 1999) or the Hamming distance (Calonder, Lepetit et Strecha, et al. 2010). For each feature in the scene, one must find its corresponding feature in the database of model features. This is equivalent to finding the nearest neighbour of the scene feature from all model features in the descriptor space. To this end, we use an exhaustive search (Calonder, Lepetit et Strecha, et al. 2010), an approximate kd-trees search (Beid et Lowe 1997) or a fast approximate nearest neighbour searches in high dimensional spaces (FLANN, see (Muja et Lowe 2009)). To prevent false matching, a threshold is used either on the distance value (Bay, Ferraris et Van Gool 2005) or on the distance ratio between the first two nearest neighbours (Lowe 2004). To avoid the threshold parameter, one can use PROSAC (Chum et Matas 2005) to find point correspondences. It is an improved version of RANSAC (Fischler et Bolles 1981), which relies on similarity measurement of point correspondences to generate hypothesis samples.

From another point of view, feature matching can be regarded as a problem of classification of feature descriptors. In that case, a class is defined as the set of views of a model feature under different transformations. Classes are trained offline and scene features are classified online. Two features belonging to the same class establish a matching. Random trees (Amit et Geman 1997) and random ferns (Ozuysal, et al. 2010) have been used and gave good results.

3.3.3   Geometric based localization

Unlike texture-based methods, geometry-based localization techniques do not rely on any photometric information to establish feature correspondences, or to directly find the camera pose. Since no colour information is used, these approaches can register information in different representations. For example, the same object being painted in different colours can be aligned with its CAD model without any previously defined colour. Raster paper maps can be registered with information from Geographical Information Systems (GIS). An infrared image of a scene can be aligned with its visual appearance, etc. Due to the lack of discriminative information, methods based on geometric information are often more computationally expensive and thus only few works have been proposed for real-time applications, e.g. Augmented Reality (AR). Therefore, the following of this section is not limited to real-time methods in order to give a wider view of what techniques are available even if they might not be applicable in our case.

In 2D images, geometric quantities are points, edges, regions (or shapes), etc. In the following, we distinguish between region-based approaches, line segment based and point based approaches.

3.3.3.1   REGION-BASED APPROACHES

A 3D object usually forms a region (or a shape) in a 2D image. Considering that regions are the most complex geometric structures in 2D images, one can obtain more information than edges or points to perform registration. As a consequence, many texture-less registration methods rely on the shape or the contour of regions.

To register planar objects, (Ghostasby, Stockman et Page 1986) use regions mass centers as control points and applies a point pattern matching method to solve the correspondence problem. (Flusser et Suk 1994) create a 4-dimensional affine invariant descriptor from each region. Each descriptor is associated

to its homologous mass center, which facilitates the point pattern-matching problem. (Martedi, Thomas et Saito 2013) use joints of line segments extracted from the region contour as control points. Support Vector Shape (SVS) (Van Nguyen et Porikli 2013) is a descriptor of shape constructed using Support Vector Machine (SVM) (Cortes et Vapnik 1995), where the resulting support vectors are used as control points near the contour of the shape. (Campbell et Petersson 2015) use SVS control points to boil down planar shape registration to point pattern matching. (Holtzer, et al. 2009) virtually generates different views of the model regions, then creates a Distance Transform (DT) (Rosenfeld et Pfaltz 1968) from each virtual view contours. These distance transforms are then used to train random ferns. Random ferns are efficient data structures where ferns (a small set of binary tests returning the probability for a feature to belong to a class learned during a training phase) are combined in a Bayesian way. See (Ozuysal, et al. 2010) for more details. The pose estimation problem is solved by online classification. The method requires that the target contains several regions and can achieve near real-time matching. (Rothwell, et al. 1992) propose a method to find four perspective invariant points on a general continuous concave curve. The method is applied by (Hagbi, et al. 2009) to calculate a perspective invariant signature for each concave curve in order to distinguish different concave shapes. It can estimate the perspective transformation with only one concave shape. (Donoser, Kontschieder et Bischof 2011) combine the method of (Holtzer, et al. 2009) and that of (Hagbi, et al. 2009) to work with at least one concave shape. They achieve real-time matching.

To register 3D objects, most researchers adopt a common approach. First, several 2D views of the 3D model object are virtually generated from a set of possible viewing angles and stored in a database with their corresponding poses in an offline phase. Then, during online matching the best virtual image with respect to the scene image is found by contour matching. At last, the pose corresponding to the matched model image is used as an initial value and refined by a recursive tracking process. (Choi et Christensen 2012) use chamfer matching for contour matching and particle filter for pose refinement. (Reinbacher, Ruther et Bischof 2010) propose to use a hierarchical structure to organize the virtual views in order to speed up the matching. (Holtzer, et al. 2009) treat the best contour-matching problem as a classification problem. They use the distance transforms of all virtual views to train ferns and the scene image is classified later on. As contour matching is a very essential step, some researchers aim at developing more efficient and robust algorithms. (Damen, et al. 2011) discretize the contour to form edgelets (short straight segments) and create a constellation of edgelets by casting a ray from one of the edgelets and following reflections of the ray on other edgelets. The descriptor of this constellation is composed of the parameters (reflecting angles, zig-zag length ratios) of its generating path, which are used for contour matching. BORDER (Chan, Addison Lee et Kemao 2016) is another descriptor for contour matching. It samples the contour to create a sequence of linelets (small line segments of equal length). The angles between linelets are used to calculate the contour's descriptor, which are matched by kd-trees.

3.3.3.2 LINE AND SEGMENT BASED APPROACHES

Due to noise, occlusion and broken detected lines, the detected endpoints of line segments are hardly reliable (Li, et al. 2016). This effect, coupled with over- or under-detections, makes it difficult to register line segments. (Coiras, Santamari et Miravet 2000) use extrapolation of lines to create meshes. An exhaustive search on mesh matching is adopted to find the final solution. (Guan, et al. 2009) also use lines or extrapolation of lines but convert line matching to point matching by using their intersections. (Wang, et al. 2013) transform lines to points by using their coordinates in the parametric space and thus convert the line matching to a point matching problem. But this does not work for affine transformations. (Long, Jiao et Wang 2014) model each line segment as a 6D vector and employ Gaussian Mixture Model and Expectation-Maximization to register the set of high dimensional vectors. This method is used to

register a map from an aerial image. But it cannot converge when the rotational angular difference between two targets is larger than 40°. (Gros, Bournez et Boyer 1998) use descriptors constructed by neighbouring line segments for similarity or affine transformations. They calculate transformations between matched descriptors and find clusters of these transformations in parametric space. Line Signatures (LS) (Wang, Neumann et You 2009) create an 11-dimension descriptor for each line segment by using its 5 neighbouring segments. They deal with affine transformations and use a hash-table for matching. The BOLD descriptor (Tombari, Franchi et Di Stefano 2013) is a vector containing two angles between two line segments and the line connecting their middle points. BOLD descriptors are matched with the help of kd-trees in order to find correspondences. This method is not affine invariant since angles change under affine transformation.

3.3.3.3   3D MODEL-BASED REGISTRATION

Another possibility to register images and models is to rely on 3D models. Historically, 3D object detection has been achieved by relying on:

- Edge detection: in a pre-processing step edges are extracted offline from the 3D model. At runtime, edges at detected in the image and are matched with the pre-processed edges. Examples of such methods include (Harris et Stennet 1990) (Klein et Murray, Full-3D Edge Tracking with a Particle Filter 2006) (Lowe 1991). Their drawbacks are that they are sensitive to large occlusions and clutter.
- Keypoints: points of interest are detected in images and matched with keypoints detected in a pre-process step on 3D models. Keypoints can be relatively easily extracted but these methods do not work for poorly textured objects (such as buildings). Examples of these methods include (Vacchetti, Lepetit et Fua 2004) (Wagner, et al. 2008).
- A combination of edges and keypoints (Rosten et Drummond 2005) or stereo information (Pauwels, et al. 2013). However, extracting and matching edges remains delicate and requiring stereo information limits the applicability of a 3D tracker.
- Silhouette extraction (Prisacariu, Segal et Reid 2012) or contour combined with edges (Chliveros, Pateraki et Trahanias 2013). These approaches fail in the case of partial occlusions.

Recently, some methods investigated how to detect or recognize 3D objects in images or to compute a 6D pose (position and orientation) of a 3D object in an image. In order to achieve these goals, most methods rely on some reconstruction of the 3D environment. This reconstruction can be obtained by different techniques:

- RGB-D cameras: these special cameras (like the Microsoft Kinect for example) can obtain classical "RGB" images but also provide a depth image of the scene currently viewed by the device. There are different technologies of RGB-D cameras but the outcome is classically a depth image that can be registered with the RGB image and that provides for each pixel of the RGB image the depth information (representing the distance between the device and the environment at this pixel). Using the Depth images, it is thus possible to reconstruct a 3D version of the environment. RGB-D sensors nevertheless have a quite limited range of operation (usually around 10m) and are not usable for building-like structures. Approaches using RGB-D cameras perform object detection in different ways such as, voting based on pairs of 3D points and normals (Salas-Moreno, et al. 2013), use template-based representations of objects (Hinterstoisser, et al. 2012) or local patches (Brachman, et al. 2014).
- Computer Vision techniques like SLAM (Simultaneous Localization and Mapping) or SfM (Structure from Motion). SLAM methods use normal (i.e. non RGB-D) cameras and use

succesive images from the camera to build on the fly a 3D version on the environment (Klein et Murray 2007) (Newcombe, Lovegrove et Davison 2011). An issue with these methods is that they do not work well in large environments and are also prone to failure with dynamic scenes.

- Using known 3D models of objects that have to be recognized in the scene. In this case, the application needs the 3D models of the objects in advance. Examples of such methods use contours as parts of 3D objects (Payet et Todorovic 2011); learn 3D parts from CAD models (Lim, Khosla et Torralba 2014); perform 3D tracking through part-based particle filtering (Xiang, et al. 2014); use the 3D Deformable Part Model (Pepik, et al. 2012); or use convolutional neural networks to learn 3D poses from model parts (Crivellaro, et al. 2015).

Since buildings are at the core of this deliverable of the B2S project we do not detail methods using RGB-D sensors or relying on SLAM methods, which typically do not work on large outdoor environments. Some details on these methods can nevertheless be found in Deliverable D4.3 In the following we briefly detail the last kind of methods, even if we do not typically have in advance the 3D models of the buildings that are to be studied.

3.3.4   Conclusion

In this section, we presented the classical approaches used to perform registration: either by relying on texture or on using 3D models. Nevertheless, the texture-based approaches cannot be used in the context of the B2S project where we rely on thermal IR images. Indeed, as mentioned above texture-based approaches usually rely on the detection and description of feature points that are computed from gradients of colour or intensities of grayscale values. As a consequence, these techniques cannot be directly applied in our case. The same goes for image-model registration techniques, where 3D models are registered with classical RGB images. This registration again relies on the detection in the images of features (edges, points, etc.) that may not be present in thermal IR images. Of course, the RGB-D techniques relying on depth cameras are mentioned here for the sake of completeness but cannot be used in B2S since there is no device capable of offering both thermal IR and RGB-D images at the same time.

In order to be able to register RGB and thermal IR images, some specific techniques may be found in the literature that we detail in the next section.

3.4   Referencing thermal images

There has been relatively little attention from the computer vision community regarding the geometrical calibration of thermal cameras and registration of IR images with classical RGB images or 3D models. In the remainder of this section we first present the difficulties of thermal cameras calibration and some proposed solutions. Then we tackle the problem of registration of thermal images with classical RGB images before focusing on methods to match IR images with 3D models.

3.4.1   Thermal Cameras Calibration

In Section 3.2.4, we presented the concept of camera calibration that leads to the computation of the intrinsic parameters of a camera. The interest of calibrating a camera is that once the intrinsic parameters are known, it is possible to remove the distortions from all the images captured by the camera (Figure 39).

An issue one faces with thermal cameras is that it is quite complex to apply the classical camera calibration techniques. Indeed, since classical targets (like the checkerboard on Figure 39) have constant temperature they cannot be easily detected in thermal images. As a consequence, in order to calibrate a thermal camera one as to build a calibration target visible in thermal images.

Figure 39: Distortion removal from an image. (Left) Original image captured with a camera. (Right) Undistorted image. Note the bottom of the whiteboard that is curved in the left (original) image and straight in the right (rectified) image. Source MathWorks[9]

To the best of our knowledge, very few papers focused on the issue of thermal camera calibration. (Lagüela, et al. 2011) propose a technique to calibrate a thermal camera based on a grid of burning lamps. They measure the accuracy of their system by using a custom-made artifact composed of five spheres made out of a special thermoplastic polyoxymethylene called Delrin and seven cubes of different sizes painted with silver paint and with black stickers attached to them. They tested their system on three thermal cameras. Their setup offer good accuracy but proves very difficult to replicate due to the complexity of the custom-made targets.

(Prakash, Lee et Caelli 2006) proposed to heat a classical checkerboard (Figure 36) with a flood lamp in order to use classical techniques to calibrate thermal cameras. Because of the difference in emissivity of the black and white regions of the checkerboard, it is possible to detect it in the thermal images.

(Yamaguchi, Saito et Yachida 2017) aimed at creating a calibration target that could be seen both by a classical RGB and a thermal camera. In order to do so, they used a classical checkerboard and a special electric carpet with thermal insulation material to generate the images of Figure 40. As a consequence, they could use classical techniques to calibrate both thermal and RGB cameras.

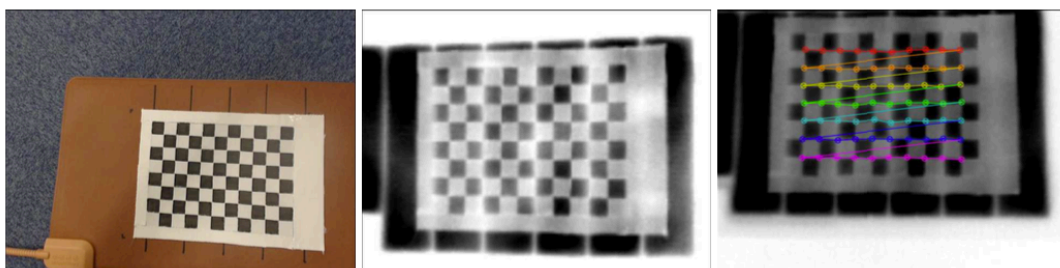*Figure 40: Setup used by (Yamaguchi, Saito et Yachida 2017) to calibrate thermal and RGB cameras. (Left) A classical checkerboard detected by the RGB camera is attached on top of a special heating board. (Left) Thermal IR image of the heated checkerboard. (Right) Illustration of OpenCV's camera calibration process with the heated checkerboard.*

---

[9] https://fr.mathworks.com/help/vision/ref/undistortimage.html

(Previtali, et al. 2013) proposed to use a custom-made calibration target composed of a large wooden panel where 40 iron nails were fixed to serve as IR calibration pattern (

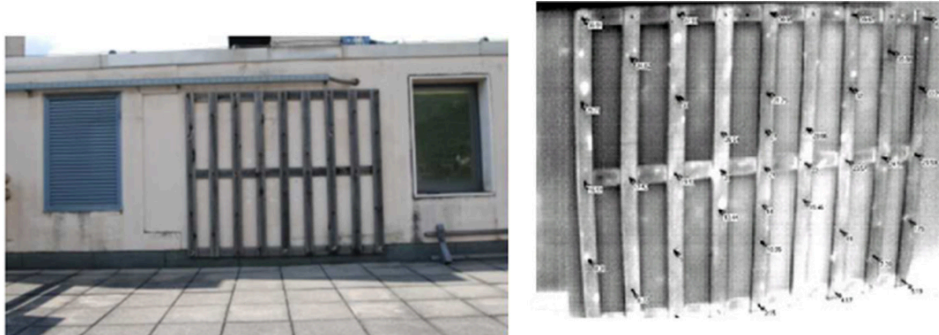Figure 41). When heated by the sun, the nails appear in the IR images and can be used to perform the calibration.

Figure 41: Wooden panel with iron nails used as a pattern for thermal camera calibration. From (Previtali, et al. 2013).

Nevertheless, the 3D positions of the nails must be known in advance to compute the thermal camera intrinsic parameters. The authors used a first order theodolite to precisely measure the positions of the nails. In a second step, the nails positions were manually selected in the IR images and fed to an optimization method along with the 3D positions of the nails to compute the intrinsic parameters. As a consequence, this procedure is cumbersome (the wooden panel is very big), and requires a lot of manual intervention, which is not suitable for the B2S needs.

Some other specific calibration patterns were also proposed (Figure 42).

The problem with these approaches is that they either need very specific setups, like (Lagüela, et al. 2011), or require some specific heating devices, (Yamaguchi, Saito et Yachida 2017). We tried using a similar approach but with our thermal cameras, simply heating a checkerboard failed. Indeed, heating the checkerboard with lights failed due to the too low difference in reflectivity between the black and white squares of the checkerboard. This led to a detection failure in the computer vision stage. We also proposed to build a checkerboard made out of special reflective tape (Figure 43). But while it proved to be usable for calibrating a classical RGB camera, some of our attempts with thermal cameras remained unsuccessful (Figure 43 right). Here the problem comes from the directivity of the tape reflection that also leads to detection failure in most of the case when the view is not exactly perpendicular to the tape.

We still need to figure out a better and simpler calibration procedure that could be easy to use in the context of the B2S project: outside and onsite to make sure that the IR images would be surely usable in the registration process.
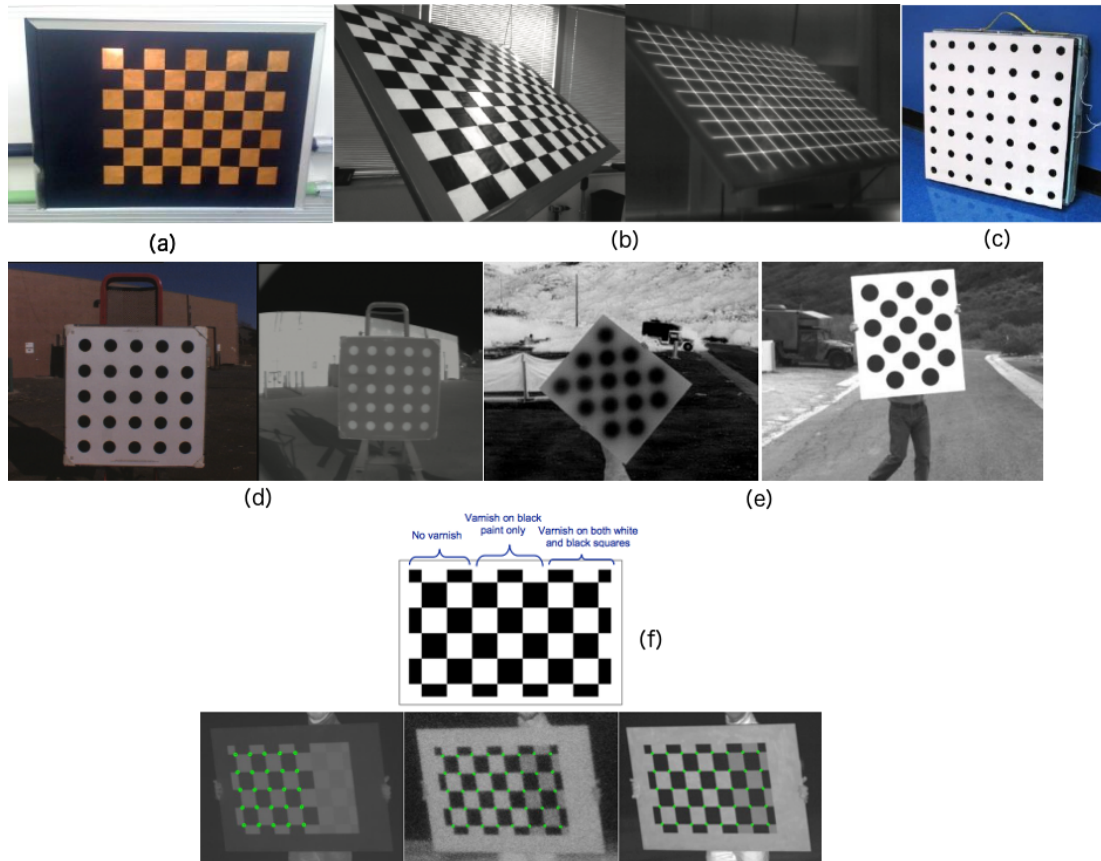
Figure 42: Some custom calibration patterns specific for thermal camera calibration. Made out of copper (Ursine, et al. 2012) (a), silicon rubber heater (St-Laurent, Prévot et Madague 2010) (b), special coated aluminium with a grid of fine wires (Rankin, et al. 2005) (c), foam (Rankin, et al. 2005) (d), special composite material called Dibond (Harguess et Strange 2014) (e), or aluminium painted with a high emissivity black paint and varnished (St-Laurent, Mikhnevich, et al. 2016) (f).

Figure 43: Left: OpenCV checkerboard detection using a custom checkerboard made out of reflective tape. Right: Detection failure using the thermal image.

3.4.2   IR-visible image registration

In this section, we focus on IR image registration with classical RGB images. The idea is to superimpose IR images on top of pictures of buildings to show their thermal quality, for an illustration see (Figure 44).

This is achieved by selecting at least 4 points on a planar surface in the RGB image (Figure 44 left) and the same corresponding points in the thermal IR image (Figure 44 centre). A correspondence between those points is then established and a homography (mathematical transformation relating two images of the same planar surface) is computed. Finally, we apply a perspective transformation to the thermal IR image and blend it (Figure 44 right) onto the RGB image (since, most of the time, it has a higher resolution).
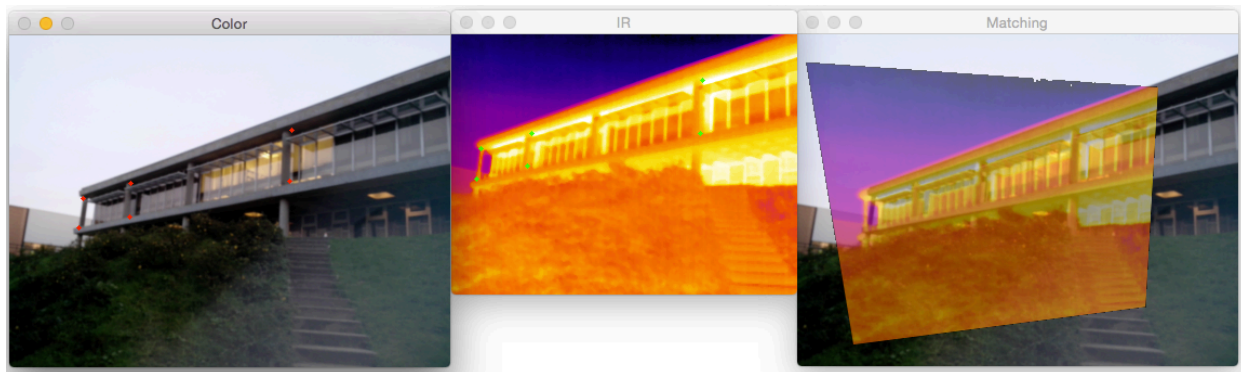

Figure 44: Registration between RGB and thermal images. Left: RGB image. Middle: Thermal image of the same building. Right: Blending of the Thermal image on top of the RGB image.

The main issue with IR-RGB registration is that the features (see Section 3.3.2) detected in an RGB image are completely different from those of an IR image of the same scene (Figure 45).

It should be noted that the misregistration problem has probably multiple sources: the most obvious being the difference in terms of gradients in the RGB and thermal images (remember that most feature points detectors and descriptors use colour gradients that are very different in the two images); but it is also worth noting that in general thermal images have a much lower resolution than RGB images. This obviously alters the quality of the features and their descriptors in thermal images. Moreover, and in the context of the B2S project, it should be noted that building facades also contain a lot of repetitive patterns (windows, doors, etc., see an example in Figure 45) and that this is a real issue for matching algorithms that do not deal well with symmetries and repetitions.

Figure 45: Corresponding SIFT features from two images of the same building. Left: Thermal image. Right: RGB image. The blue lines represent the computed correspondences between keypoints extracted from the thermal and the RGB images. One can observe that many of these correspondences are false (a keypoint in the thermal image does not correspond to the same point in the RGB image). Source (Liu et Seipel 2015).

Since, classical matching methods fail to register images of the same scene but of different modes (RGB, thermal, etc.), some research has been devoted to solve this issue. Most researchers try to find features that are present in both images and thus that do not depend on pixels gray levels since they differ greatly in thermal and RGB images.

In the following, we first detail methods relying on segments and line to perform the thermal-RGB registration. Then we focus on hybrid methods that use segments and additional information to perform the matching.

3.4.2.1 LINE-BASED THERMAL IR-RGB IMAGE MATCHING

(Dana et Anandan 1993) make the assumption that some of the segments detected in one of the image (e.g. the RGB image) are present and detected in the two images. As a consequence, they compute an affine transformation between the two images using a pyramidal approach and a coherence hypothesis. At each level of the pyramid, segments are detected and an affine transformation is computed based on a mean squared error (MSE). In order to refine the result and use a higher level of the pyramid, incoherent segments are then discarded.

A common issue when relying on segments extracted from an image is that they frequently appear fragmented, incomplete or not in the same position in the different images of the same object. Another issue with segments is that, since a segment from image A can potentially be match to any other segment in image B, the number of potential matches is often very high.

In order to limit the drawbacks of using segments alone, some authors proposed to use couples, (Gros, Bournez et Boyer 1998) or triplets (Coiras, Santamaría et Miravet 2000) of intersecting segments. The interest of using triplets of segments is that when triplets are matched, an affine transformation may be computed. The limits of this method are that these authors used thermal and RGB images of comparable resolutions, which is usually not the case, and that they used a relatively low number of segments (around 100), which is typically not the case when using urban scenes. Moreover, it seems that the method requires a comparable number of segments in the two images.

In (Ribarić et Mihalić 2007), the authors aimed at detecting features (edges) that could be present in both RGB and thermal IR images. They detected feature points in both images, filtered them to keep only those larger than an arbitrary length (16 pixels) and connected them to form edges. In a second step, they needed to keep only compatible features. In order to do so, they looked for points that were located in a "similar" square in both images and they declared two edges to be compatible if they had "similar" starting point, end point and length. Then they computed the affine transformation between both sets of edges. Their method only work when (1) both RGB and thermal IR images are of similar resolution (not generally the case where you have to severely reduce the RGB image to scale it down to the size of the thermal IR image) and (2) when the images were taken from a very similar point of view. When the transformation between both images is too important the matching fails.

In (Ribarić, Marčetić et Vedrina 2009) the authors used an idea similar to (Coiras, Santamaría et Miravet 2000) to match between edges detected in both RGB and thermal IR images. They applied the Canny operator (Canny 1986) to detect edges in both images, group them into line segments (by applying the polarized Hough transform (Illingworth et Kittler 1988)) to reduce the number of features. Then they used a brute force method to estimate an affine transformation to register both images. Again, here both images must have comparable resolutions and almost the same viewpoint.

In a similar way, (Han, Pauwels et de Zeeuw 2011) chose to match lines extracted from visible and IR images using the Hough transform. They classified the extracted vertical and horizontal lines before matching them (vertical with verticals and horizontals with horizontals). Here again, the method only works when the viewpoints of the visible and infrared cameras are very similar.

3.4.2.2   HYBRID METHODS FOR THERMAL IR-RGB IMAGE MATCHING

As mentioned in the previous section, the drawback of relying on line segments to perform the registration is that the RGB and thermal IR images need to be very similar in terms of resolution and of viewpoint. To overcome these limitations, it has been proposed to rely on more complex features than just lines.

In (Liu et Seipel 2015) the authors aimed at registering visible and thermal IR images from building facades. They assumed that the images contain some characteristic quadrilateral elements such as windows or doors. They proposed to use quadrilateral features instead of using lines to match the two images. They obtained good results but their method required both images to be of good quality. Moreover, their algorithm may fail when facades do not provide sufficient quadrilateral characteristics or when the detection fail (e.g. when windows are merged into a larger quadrilateral).

Building upon previous work (see Section 3.4.2.1), (Han, Pauwels et de Zeeuw 2013) proposed a modified variant of their algorithm using not only straight lines but a hybrid feature of lines and points. They use a two-stage procedure in which they first use line features to establish a global but approximate transformation between the two images. This global transformation is then used to bootstrap a more accurate, locally adaptive transformation that is based on a windowed optimization of feature point matching. Their approach seems interesting but fail on some images due to the poor quality of the line detection algorithm. They also need to detect stable feature points in the IR and visible images, which is hardly the case in our context; otherwise, we could have used state-of-the-art image registration techniques.

3.4.3   Thermal IR images-model registration

To the best of our knowledge, the only model-based registration technique (see Section 3.4.1) using thermal IR images is that of (Previtali, et al. 2013). These authors propose an accurate mapping of thermal IR images onto a detailed 3D model of real buildings by combining different surveying techniques like photogrammetry or Terrestrial Laser Scanning (TLS). The outputs of the procedure consisted in photo-textured 3D models and ortho-images, which gave support to the precise localization of thermal defects/anomalies and to the evaluation of their extension. There are a number of prerequisites: RGB images should be captured with good natural lighting conditions, and IR data should be gathered at a time when the façade thermal radiation is highest. Their method is quite complex and involves time consuming manual operations as well as costly and also time-consuming photogrammetry techniques. It remains largely inapplicable in the context of the B2S project.

3.5   Conclusion

We have presented a thorough review of literature of techniques performing 3D automated referencing. As detailed in Section 3.3.3.3, there are numerous techniques to detect or recognize known 3D objects in images but none of them can be directly applied in the context of the B2S project. To the best of our knowledge, there has been only one attempt (see Section 3.4.3) at registering thermal IR images with 3D models.

As mentioned above, the misregistration problem between thermal IR and RGB images has multiple sources: differences in terms of gradients in the RGB and thermal images as well as in terms of image; or presence of repetitive patterns in building facades (a real issue for matching algorithms).

Indeed classical matching methods fail to register images of the same scene but of different modes (RGB, thermal, etc.), since features usually depend on pixels gray levels, which greatly differ greatly between thermal IR and RGB images.

This technique remains largely inapplicable in the context of the B2S project since the authors rely on precomputed laser scanning of the buildings composing the scene, which is out of scope of the current task.

As a conclusion, it can be noticed that we did not find in the literature any existing solution to perform thermal IR images-3D models registration and that, as of now, the task remains a scientific challenge.

As a consequence, in a first stage to allow the user to perform its quality checks we propose a manual method for the thermal IR-RGB images registration and in a second stage to perform a visualization of thermal IR images directly superimposed onto a 3D model of the building.

4 Conclusions

This document in its first part, presented two approaches for heat thermal transfer modelling at wall scale: the quadrupole modelling and the finite difference modelling. We have verified that both models are able to predict correctly the surface temperatures in the heat transfer regime of thick wall. These models were then used for the direct and the inverse approaches.

Then, the direct detailed building modelling based on the finite difference method and taken into account defects was presented and validated. It is a model where the spatial discretization of the building envelope can be adapted to the size and the location of the defect. The preliminary analysis was done by considering defects as materials with different properties or thicknesses than initially planned during the design stage on the entire envelope and also a local defect like a lack of insulation. First applications showed the potential of this new model to integrate the considered defects. The next step will be to propose an experimental in-situ protocol to detect the defect by TIR measurements and to apply it on the monitored building in Nantes (deliverables D2.3 and D7.2). Then, to carry comparison between simulations with defects and measurements conducted on the monitored building.

Finally, the inverse modelling approach was presented. The aim of the work done is, firstly to characterize the thermal properties of walls in lab conditions and secondly, to understand in which situations this method could be used to characterize buildings envelope under realistic conditions. Two methods were presented based on experimental measurements (temperatures and heat flux) and numerical simulations (Quadrupole modelling and the finite difference modelling). The results show that the inverse model is able to estimation thermophysical properties of a multilayered tested sample. The next step will be to apply this model to other configurations in the framework of Built2Spec project.

Then the second part presented first a state of the art on image-image and image-model referencing along with some attempt to solve IR/model referencing and IR/visible referencing in the case of Build2Spec use cases. First the problem position in Build2Spec context is stated: align a set of 2D thermal images from a building (or buildings) onto a 3D model (or models) of the same building in order to visualize its thermal quality. Then basis of computer vision and state of the art on pose calculation methods based on textures and geometries are presented. This review aimed in showing the literature methods for the RGB image to calculate the pose w.r.t. an image and/or a 3D model and to register this image towards a corresponding 3D model. The following sections are dedicated to the specificity of IR image compared to RGB images. A review of the literature to register IR image on RGB image is presented but are not usable in the Built2Spec context.

As the tests on IR images in this part show, the classic solutions usually working with visible images are not working anymore on IR images and the IR image alignment with a 3D model cannot be done automatically. Then a manual procedure to register IR and/or visual images onto a 3D BIM model has been developed to allow the user to perform its quality checks.

5 Bibliography

Abdel-Aziz, Y. I., and H. M. Karara. 1971. "Direct linear transformation from comparator coordinates into object space coordinates in close-range photogrammetry." *Proceedings of the Symposium on Close-Range Photogrammetry.* Falls Church, VA: American Society of Photogrammetry. 1-18.

Aissani, A., A. Chateauneuf, J-P. Fontaine, and P. Audebert. 2016. "Quantification of workmanship insulation defects and their impact on the thermal performance of building facades." *Applied Energy* 272-284.

Amit, Y., and D. Geman. 1997. "Shape quantization and recognition with randomized trees." *Neural computation* 9(7): 1545-1588.

Asdrubali, F., F. D'Alessandro, G. Baldinelli, and F. Bianchi. 2014. "Evaluating in situ thermal transmittance of green buildings mansories a case study." *Case Stud Constr Mater 1* 53-59.

Awrangjeb, M., G. Lu, and C. S. Fraser. 2012. "Performance comparisons of contour-based corner detectors." *IEEE Transactions on Image Processing* 21(9): 4167-4179.

Azuma, Ronald T. 1997. "A survey of augmented reality." *Presence: Teleoperators and virtual environments* 6 (4): 355-385.

Ballesta, M., A. Gil, O. Reinoso, and O. M. Mozos. 2008. "Evaluation of interest point detectors for visual SLAM." *International Journal of Factory Automation, Robotics and Soft Computing* 4: 86-95.

Bay, H., A. Ess, T. Tuytelaars, and L. Van Gool. 2008. "Speeded-Up Robust Features (SURF)." Edited by Elsevier Science Inc. *Comput. Vis. Image Underst.* 110(3): 346-359.

Bay, H., V. Ferraris, and L. Van Gool. 2005. "Wide-baseline stereo matching with line segments." *IEEE Computer Society Conference on Computer Vision and Pattern Recognition (CVPR'05)*, 329-336.

Beid, J. S., and D. G. Lowe. 1997. "Shape indexing using approximate nearest-neighbour search in high-dimensional spaces." *Computer Vision and Pattern Recognition, 1997. Proceedings., 1997 IEEE Computer Society Conference on.* 1000-1006.

Bierlaire, Michel. 2013. *Introduction à l'optimisation différentiable.* Presses polythchniques et universtiaires romandes.

Billinghurst, M., A. Clark, and G. Lee. 2015. "A Survey of Augmented Reality." *Foundations and Trends in Human-Computer Interaction* 8 (3): 73-272.

Borderon, J., R. Lahrech, J-R. Millet, and S. Tasca-Guernouti. 2013. "Influence of fiels data quality on the modeling of residential buildings with dynamic simulation tool." *13th Conference of International Building Performance Simulation Association, France Chambéry* 26-28.

Botterill, T., S. Mills, and R. D. Green. 2009. "New Conditional Sampling Strategies for Speeded-Up RANSAC." *British Machine Vision Conference.* 1-11.

Bouyer, J., C. Inard, and M. Musy. 2011. "Microclimatic coupling as a solution to improve building energy simulation in an urban context." *Enery Building* 1549-1559.

Brachman, E., A. Krull, F. Michel, S. Grumhold, J. Shotton, and C. Rother. 2014. "Learning 6D Object Pose Estimation Using 3D Object Corrdinates." *European Conference on Computer Vision.*

Braiek, A., M. Karkri, A. Adili, L. Ibos, and S. B. Nasrallah. 2017. "Estimation of the thermophysical properties of date palm fibres/gypsum composite for use as insulation materials in building." *Energy and Bulidings* 140: 368-279.

Calonder, M., V. Lepetit, C. Strecha, and P. Fua. 2010. "BRIEF : Binary Robust Independent Elementary Features." *In European Conference on Computer Vision.*

Calonder, M., V. Lepetit, M. Ozuysal, T. Trzcinski, C. Strecha, and P. Fua. 2012. "BRIEF: Computing a Local Binary Descriptor Very Fast." *IEEE Trans. Pattern Anal. Mach. Intell.* 34(7): 1281-1298.

Campbell, D., and L. Petersson. 2015. "An adaptive data representation for robust point-set registration and merging." *IEEE International Conference on Computer Vision.* IEEE. 4292-4300.

Canny, J. 1986. "A computational approach to edge detection." *IEEE Transactions on Pattern Analysis and Machine Intelligence* (IEEE) 8 (6): 679-698.

Chan, J., J. Addison Lee, and Q. Kemao. 2016. "BORDER: An Oriented Rectangles Approach to Texture-Less Object Recognition ." *IEEE Conference on Computer Vision and Pattern Recognition.* IEEE. 2855-2863.

Chliveros, G., M. Pateraki, and P. Trahanias. 2013. "Robust Multi-Hypothesis 3D Object Pose Tracking." *International Conferene on Computer Vision (ICCV).*

Choi, C., and H. I. Christensen. 2012. "3D textureless object detection and tracking: An edge-based approach." *IEEE/RSJ International Conference on Intelligent Robots and Systems.* IEEE. 3877-3884.

Chum, O., and J. Matas. 2005. "Matching with PROSAC - Progressive Sample Consensus." *Proc. of the 2005 IEEE Computer Society Conference on Computer Vision and Pattern Recognition.* 220-226.

Coiras, E., J. Santamari, and C. Miravet. 2000. "Segment-based registration technique for visual-infrared images." *Optical Engineering* 39 (1): 282-289.

Coiras, Enrique, Javier Santamaría, and Carlos Miravet. 2000. "Segment-based registration technique for visual-infrared images." *Optical Engineering* 39 (1): 29.

Cortes, C., and V. Vapnik. 1995. "Support-Vector Networks." *Machine Learning* 20 (3): 273-397.

Crivellaro, A., M. Rad, Y. Verdie, K.-M. Yi, P. Fua, and V. Lepetit. 2015. "A Novel Representation of Parts for Accurate 3D Object Detection and Tracking in Monocular Images." *IEEE International Conference on Computer Vision (ICCV).*

Damen, D., A. Gee, A. Calway, and W. Mayol-Cuevas. 2011. "Detecting and localising multiple 3D objects: A fast and scalable approach ." *IROS Workshop on Active Semantic Perception and Object Search in the Real World.* 1-6.

Dana, K., and P. Anandan. 1993. "Registration of visible and infrared images." *Optical engineering and Photonics in Aerospace Sensing* 2-13.

Datta, A., J.-S. Kim, and T. Kanade. 2013. "Accurate Camera Calibration using Iterative Refinement of Control Points." *Workshop of the IEEE 21th International Conference on Computer Vision.* IEEE. 1-7.

Denis Maillet, Stephane Andre, Jean-Christophe Batsale, Alain Degiovanni, and Christian Moyne. 2000. *Thermal Quadrupoles:solving the heat equotion through integral transforms.*

Denton, J. A., and J. R. Beveridge. 2007. "An algorithm for projective point matching in the presence of spurious points." *Pattern Recognition* 40 (2): 586-595.

Derbal, Radhouan. 2014. *Développement d'une méthode de caractérisation thermique.* Béthune: Université d'Artois.

Donoser, M., and H. Bischof. 2006. "Efficient maximally stable extremal region (MSER) tracking." *2006 IEEE Computer Society Conference on Computer Vision and Pattern Recognition.* 553-560.

Donoser, M., P. Kontschieder, and H. Bischof. 2011. "Robust planar target tracking and pose estimation from a single concavity." *IEEE International Symposium on Mixed and Augmented Reality.* IEEE. 9-15.

Fiala, M. 2005. "ARTag, a fiducial marker system using digital techniques." *IEEE Computer Society Conference on Computer Vision and Pattern Recognition.* IEEE. 590--596.

Fischler, M. A., and R. C. Bolles. 1981. "Random Sample Consensus: A Paradigm for Model Fitting with Applications to Image Analysis and Automated Cartography." *Commun. ACM* 24(6): 381-395.

Flusser, J., and T. Suk. 1994. "A moment-based approach to registration of images with affine geometric distortion ." *IEEE Transactions on Geoscience and Remote Sensing* 32 (2): 382-387.

Forssén, P. E., and D. G. Lowe. 2007. "Shape descriptors for maximally stable extremal regions." *IEEE 11th International Conference on Computer Vision.* 1-8.

Fox, M., S. Goodhew, and P. De Wilde. 2016. "Building defect detection: External versus internal thermography." *Building and Environment* 317-331.

Ghostasby, A., G. C. Stockman, and C. V. Page. 1986. "region-based approach to digital image registration with subpixel accuracy." *IEEE Transactions on Geoscience and Remote Sensing* 3: 390-399.

Grompone von Gioi, R., J. Jakubowicz, J.-M. Morel, and G. Randall. 2010. "LSD: a fast line segment detector with a false detection control." *IEEE transactions on pattern analysis and machine intelligence* 32(4): 722-732.

Gros, P., P. Bournez, and E. Boyer. 1998. "Using local planar geometric invariants to match and model images of line segments." *Computer Vision and Image Understanding* 69 (2): 135-155.

Guan, W., L. Wang, J. Mooser, S. You, and U. Neumann. 2009. "Robust pose estimation in untextured environments for augmented reality applications ." *IEEE International Symposium on Mixed and Augmented Reality.* IEEE. 191-192.

Hagbi, N., O. Bergig, J. El-Sana, and M. Billinghurst. 2009. "Shape recognition and pose estimation for mobile augmented reality ." *IEEE International Symposium on Mixed and Augmented Reality.* IEEE. 65-71.

Han, J., E. Pauwels, and P. de Zeeuw. 2011. "Visible and Infrared Image Registration Employing Line-Based Geometric Analysis." *Proceedings of the 2011 international conference on Computational Intelligence for Multimedia Understanding.* 114-125.

Han, J., E. Pauwels, and P. de Zeeuw. 2013. "Visible and infrared image registration in man-made environments employing hybrid visual features." *Pattern Recognition Letters* 34 (1): 42-51.

Harguess, J., and S. Strange. 2014. "Infrared Stereo Calibration for Unmaned Ground Vehicle Navigation."

Harris, C., and C. Stennet. 1990. "RAPID A Video Rate Object Tracker." *BMVC British Machine Vision Conference.*

Harris, C., and M. Stephens. 1988. "A combined corner and edge detector." *Alvey vision conference.* 50.

Hartley, R., and A. Zisserman. 2003. *Multiple View Geometry in computer vision.* Cambridge: Cambridge University Press.

Hénon, A., P. Mestayer, D. Groleau, and J. Voogt. 2011. "High resolution thermo-radiative modeling of an urban fragment in Marseilles city center during the UBL-ESCOMPTE campaign." *Building Envrironment* 1747-1764.

Hénon, A., P. Mestayer, J.-P. Lagouarde, and J. Voogt. 2012. "An urban neighborhood temperature and energy study from the CAPITOUL experieement with the SOLENE model - Part I: analysis of flux contributions." *Theor Appl. CLim. 110* 177-196.

Hénon, A., P. Mestayer, J.-P. Lagouarde, and J. Voogt. 2012. "An urban neighborhood temperature and energy study from the CAPITOUL experiment with the SOLENE model - PArt 2: influence of building surface heterogeneities." *Theor. Appl. CLim.* 197-208.

Heyl, J. S. 2013. "kd Match: A Fast Matching Algorithm for Sheared Stellar Samples." *arXiv preprint.*

Hinterstoisser, S., C. Cagniart, S. Ilic, P. Sturm, N. Navad, P. Fua, and V. Lepetit. 2012. "Gradient Response Maps for Real-Time Detection of Textureless Objects." *Pattern Analysis and Machine Intelligence* 34 (5): 876-888.

Holtzer, S., S. Hinterstoisser, S. Ilic, and N. Navab. 2009. "Distance transform templates for object detection and pose estimation ." *IEEE Conference on Computer Vision and Pattern Recognition.* IEEE. 1177-1184.

Illingworth, I., and J. V. Kittler. 1988. "A survey of the Hough transform." *Computer Vision Graphics and Image Processing* 44 (1): 87-116.

ISO, E. 6946. 2007. *Building components and building elements. Thermal resistance and thermal transmittance.* Calculation method.

Jayamaha, S.E.G., N.E. Wijeysundera, and S.K. Chou. 1996. "Measurement of the heat transfer coefficient for walls." *Building and Environment* 399-407.

Kato, H., and M. Billinghurst. 1999. "Marker tracking and HMD calibration for a video-based augmented reality conferencing system." *2nd IEEE and ACM International Workshop on Augmented Reality.* IEEE Computer Society.

Kenneth, Levenberg. 1944. "A method for the solution of certain non-linear problems in least squares." *Quarterly Journal of Applied Mathmatics* 2 (2): 164-168.

Klein, G., and D. Murray. 2006. "Full-3D Edge Tracking with a Particle Filter." *BMVC British Machine Vision Conference.*

—. 2007. "Parallel Tracking and Mapping for Small AR Workspaces." *IEEE International Symposium on Mixed and Augmented Reality.*

Lagüela, S. González-Jorge, H. Armesto, J. Arias, P. 2011. "Calibration and verification of thermographic cameras for geometric measurements." *Infrared Physics and Technology* 54 (2): 92-99.

Lagüela, S., H. Gonzàlez-Jorge, J. Armesto, and P. Arias. 2011. "Calibration and verification of thermographic cameras for geometric measurements." *Infrared Physics and Technology* 54: 92-99.

Lamdan, Y., and H. J. Wolfson. 1991. "On the error analysis of geometric hashin." *IEEE Computer Society Conference on Computer Vision and Pattern Recognition.* IEEE. 22-27.

Lang, D., D. W. Hogg, K. Mierle, M. Blanton, and S. Roweis. 2010. "Astronomy.net: Blind astrometric calibration of arbitrary astronomical images." *The Astronomical Journal* 139 (5): 1782.

Li, K., J. Yao, M. Lu, Y., Wu, T. Heng, and Y. Li. 2016. "Line segment matching: A benchmark." *IEEE Winter Conference on Applications of Computer Vision.* IEEE. 1-9.

Lim, J., A. Khosla, and A. Torralba. 2014. "FPM: Fine Pose Parts-Based Model with 3D CAD Models." *European Conference on Computer Vision (ECCV).*

Liu, Fei, and Stefan Seipel. 2015. "Infrared-visible image registration for augmented reality-based thermographic building diagnostics." *Visualization in Engineering* (Springer) 3 (1): 16.

Long, T., W., He, G. Jiao, and W. Wang. 2014. "Automatic line segment registration using Gaussian mixture model and expectation-maximization algorithm." *IEEE Journal of Selected Topics in Applied Earth Observations and Remote Sensing* 7 (5): 1688-1699.

Lowe, D. G. 2004. "Distinctive Image Features from Scale-Invariant Keypoints." *Int. J. Comput. Vision.* 91-110.

Lowe, D. G. 1991. "Fitting Parameterized Three-Dimensional Models to Images." *Pattern Analysis and Machine Intelligence* 13 (5): 441-450.

—. 1999. "Object recognition from local scale-invariant features." *Computer vision, 1999. The proceedings of the seventh IEEE international conference on.* 1150-1157.

M.Faye, B. Lartigue, and V. Sambou. 2015. "A new procedure for the experimental measurement of the effective heat capacity of wall elements." *Energy and Buildings* 103: 62-69.

Malys, L. 2012. *Évaluation des impacts directs et indirects des façades et des toitures végétales sur le comportement thermique des bâtiments (Ph. D.Thesis). Ecole Centrale de Nantes, Nantes, France.*

Maquart, W. D. 1963. "An Algorithm for Least-Squares Estimation of Nonlinear Parameters." *Journal of the Society for Industrial and Applied Mathematics* 11 (2): 431-441.

Marchand, E., H. Uchiyama, and F. Spindler. 2016. "Pose estimation for Augmented Reality: A Hands-on Survey." Edited by IEEE. *IEEE Transactions on Visualization and Computer Graphics* 22 (12): 2633--2651.

Martedi, S., B. Thomas, and H. Saito. 2013. "Region-based tracking using sequences of relevance measures ." *IEEE International Symposium on Mixed and Augmented Reality.* IEEE. 1-6.

Mathworks. 2017. *https://fr.mathworks.com/.* Accessed 04 04, 2017. https://fr.mathworks.com/help/optim/ug/lsqnonlin.html.

Mestayer, P., J.-M. Rosant, F. Rodriguez, and J.-M. Rouaud. 2011. "The experimental campaign FluxSAP 2010: climatological measurements over a heterogeneous urban area." *Int. Assoc. Urban Clim. 40* 22-30.

Moreels, Pierre Perona, Pietro. 2007. "Evaluation of Feature Detectors and Descriptors based on 3D Objects." Edited by Springer. *International Journal of Computer Vision* 73 (3): 263-284.

Muja, Marius, and David G. Lowe. 2009. "Fast Approximate Nearest Neighbors with Automatic Algorithm Configuration." *International Conference on Computer vision Theory and Applications (VISAPP'09).*

Musy, M., L. Malys, B. Morille, and C. Inard. 2015. "The use of Solene-Microclimat model to assess adaptation strategies at the district scale." *Urban Climate 14* 213-22.

Myatt, D. R., P. H. S. Torr, S. J. NAsuto, J. M. Bishop, and R. Craddock. 2002. "NAPSAC: high noise, high dimensional robust estimation ." *British Machine Vision Conference.* 458-467.

Naimark, L., and E. Foxlin. 2002. "Circular data matrix fiducial system and robust image processing for a wearable vision-inertial self-tracker." *Proceedings of the 1st International Symposium on Mixed and Augmented Reality.* IEEE Computer Society.

Nakai, T., K. Kise, and M. Iwamura. 2006. "Use of Affine Invariants in Locally Likely Arrangement Hashing for Camera-based Document Image Retrieval." *7th International Conference on Document Analysis Systems.* 541-552.

Newcombe, R., S. Lovegrove, and A. Davison. 2011. "DTAM: Dense Tracking and Mapping in Real-Time." *International Conference on Computer Vision (ICCV).*

Ni, K., H. Jin, and F. Dellart. 2009. "GroupSAC: Efficient Consensus in the Presence of Groupings." *IEEE International Conference on Computer Vision.* IEEE. 2193-2200.

Nuruzzaman, Mohammad. 2013. *Finite Difference Fundamentals in MATLAB.* Createspace.

Ozuysal, M., M. Calonder, V. Lepetit, and P. Fua. 2010. "Fast keypoint recognition using random ferns." *IEEE transactions on pattern analysis and machine intelligence* 32(3): 448-461.

Pauwels, K., L. Rubio, J. Diaz, and E. Ros. 2013. "Real-Time Model-Based Rigid Object Pose Estimation and Tracking Combining Dense and Sparse Visual Cues." *EEE Conference on Computer Vision and Pattern Recognition (CVPR).*

Payet, N., and S. Todorovic. 2011. "From Contours to 3D Object Detection and Pose Estimation." *International Conference on Computer Vision (ICCV).*

Pepik, B., M. Stark, P. Gehler, and B. Schiele. 2012. "Teaching 3D Geometry to Deformable Part Models." *IEEE International Conference on Computer Vision and Pattern Recognition (CVPR).*

Prakash, S., P. Y. Lee, and T. Caelli. 2006. "3D Mapping of Surface Temperature Using Thermal Stereo." *9th International Conference on Control, Automation, Robotics and Vision.* IEEE.

Previtali, Mattia Barazzetti, Luigi Redaelli, Veronica Scaioni, Marco Rosina, Elisabetta. 2013. "Rigorous procedure for mapping thermal infrared images on three-dimensional models of building façades." *Journal of Applied Remote Sensing* 7 (1): 19.

Previtali, Mattia, Luigi Barazzetti, Veronica Redaelli, Marco Scaioni, and Elisabetta Rosina. 2013. "Rigorous procedure for mapping thermal infrared images on three-dimensional models of building façades." *Journal of Applied Remote Sensing* 7 (1): 19.

Prisacariu, V., A. Segal, and I. Reid. 2012. "PWP3D: Real-Time Segmentation and Tracking of 3D Objects." *International Journal on Computer Vision* 98: 335-354.

Raguram, R., O. Chum, M. Pollefeys, J. Matas, and J.-M. Frahm. 2013. "USAC: A Universal Framework for Random Sample Consensus." *IEEE Transactions on Pattern Analysis and Machine Intelligence* (IEEE) 35 (8): 2022-2038.

Rankin, A., A. Huertas, L. Matthies, M. Bajracharya, C. Assad, S. Brennan, P. Bellutta, and G. Sherwin. 2005. "Unmanned ground vehicle perception using thermal infrared cameras." *Proceedings of SPIE Int. Opt. Soc. Eng. Unmanned Ground Vehicle Technology VI.* 343-358.

Rao, Singiresu S. 2009. *Engineering Optimization: Theory and Practice.* Wiley.

Reinbacher, C., M. Ruther, and H. Bischof. 2010. "Pose estimation of known objects by efficient silhouette matching ." *International Conference on Pattern Recognition.* IEEE. 1080-1083.

Ribarić, Slobodan Marčetić, Darijan Vedrina, Denis Stjepan. 2009. "A knowledge-based system for the non-destructive diagnostics of façade isolation using the information fusion of visual and IR images." *Expert Systems with Applications* 36 (2 PART 2): 3812-3823.

Ribarić, Slobodan, and Darko Mihalić. 2007. "Robust Image Registration Based on Features Extracted from Image of Edges." *Proceedings of the 30th International Convention MIPRO 2007 on Computers in Technical Systems and Intelligent Systems.* 6.

Ribarić, Slobodan, Darijan Marčetić, and Denis Stjepan Vedrina. 2009. "A knowledge-based system for the non-destructive diagnostics of façade isolation using the information fusion of visual and IR images." *Expert Systems with Applications* 36 (2 PART 2): 3812-3823.

Ribaric, Slobodan Mihalic, Darko. 2007. "Robust Image Registration Based on Features Extracted from Image of Edges." *Proceedings of the 30th International Convention MIPRO 2007 on Computers in Technical Systems and Intelligent Systems.* 6.

Rigoutsos, I., and R. Hummel. 1995. "A Bayesian approach to model matching with geometric hashing." *Computer Vision and Image Understanding* 62 (1): 11-26.

Robitu, M. 2005. *Etude de l'interaction entre le bâtiment et son environnement urbain: influence sur les conditions de confort en espaces extérieurs (Ph. D.Thesis). Ecole Polytechnique de l'Université de Nantes.*

Rosenfeld, A., and J. L. Pfaltz. 1968. "Distance functions on digital pictures ." *Pattern Recognition* 1 (1): 33-61.

Rosten, E., and T. Drummond. 2005. "Fusing Points and Lines for High Performance Tracking." *International Conference on Computer Vision.*

—. 2006. "Machine Learning for High-speed Corner Detection." *Proceedings of the 9th European Conference on Computer Vision - Volume Part I.* Graz, Austria: Springer-Verlag. 430-443.

Rosten, E., R. Porter, and T. Drummond. 2010. "Faster and better: A machine learning approach to corner detection." *IEEE transactions on pattern analysis and machine intelligence* 32(1): 105-119.

Rothwell, C. A., A. Zisserman, D. A. Forsyth, and J. L. Mundy. 1992. "Canonical frames for planar object recognition." *European Conference on Computer Vision.* Springer. 757-772.

Rublee, E., V. Rabaud, K. Konolige, and G. Bradski. 2011. "ORB: An Efficient Alternative to SIFT or SURF." *Proceedings of the 2011 International Conference on Computer Vision.* IEEE Computer Society. 2564-2571.

Salas-Moreno, R., R. Newcombe, H. Strasdat, P. Kelly, and A. Davison. 2013. "SLAM++: Simultaneous Localization and Mapping at the Level of Objects." *IEEE International Conference on Computer Vision and Pattern Recognition (CVPR).*

Shi, J., and C. Tomasi. 1994. "Good Features to Track." *Proc. of the 1994 IEEE Conference on Computer Vision and Pattern Recognition.* 593-600.

Spitz, C., L. Mora, E. Wurtz, and J. Arnaud. 2012. "Practical application of uncertainty analysis and sensitivity analysis on an experimental house." *Energy and Buildings 55* 459-470.

St-Laurent, L., D. Prévot, and X. Madague. 2010. "Fast and accurate calibration-based thermal/colour sensors registration." *10th International Conference on Quantitative InfraRed Thermography.*

St-Laurent, L., M. Mikhnevich, A. Bubel, and D. Prévost. 2016. "Passive calibration board for alignment of VIS-NIR, SWIR and LWIR images." *13th International Conference on Quantitative Infrared Thermography.*

Sztanyi, R. 2015. "Construction defects in the subsequent insulation of panel buildings." *Fascicle of Management and Technological Engineering, Annals of the oradea University.*

Tombari, F., A. Franchi, and L. Di Stefano. 2013. "BOLD features to detect texture-less objects." *IEEE International Conference on Computer Vision.* IEEE. 1265-1272.

TRNSYS. 1996. "TRNSYS Mathematical reference.Solar Energy Laboratory Madison, United States, University of Wisconsin."

Tsai, R. Y. 1987. "A Versatile Camera Calibration for High-Accuracy 3D Machine Vision Metrology Using Off-the-Shelf TV Cameras and Lenses." *IEEE Journal of Robotics and Automation* RA-3 (4): 323-344.

Uchiyama, H., and H. Saito. 2011. "Random Dot Markers." *IEEE Virtual Reality Conference.* 271--272.

Ursine, W., F. Calado, G. Teixeira, H. Diniz, S. Silvino, and R. de Andrade. 2012. "Thermal/visible autonomous stereo visio system calibration methodology for non-controlled environments." *11th International Conference on Quantitative InfraRed Thermography.*

Vacchetti, L., V. Lepetit, and P. Fua. 2004. "Stable Real-Time 3D Tracking Using Online and Offline Information." *PAttern Analysis and Machine Intelligence* 26 (10): 1385-1391.

Vam Wamelen, P. B., Z. Li, and S. S. Iyengar. 2004. "A fast expected time algorithm for the 2-D point pattern matching problem." *Pattern Recognition* 37 (8): 1699-1711.

Van Nguyen, H., and F. Porikli. 2013. "Support vector shape: A classi er- based shape representation ." *IEEE Transactions on Pattern Analysis and Machine Intelligence* 35 (4): 970-982.

VDI. 2010. *VDI Heat Atlas.* Berlin: Springer-Verlag Berlin Heidelberg.

Vinet, J. 2000. "Contribution à la modélisation thermo-aéraulique du microclimat urbain. Caractérisation de l'impact de l'eau et de la végétation sur lesconditions de confort en espaces extérieurs (Ph. D. Thesis). Université de Nantes Ecole Polytchnique de l'Université de." France.

Wagner, D., G. Reitmayr, A. Mulloni, T. Drummond, and D. Schmalstieg. 2008. "Pose Tracking from Natural Features on Mobile Phones." *IEEE International Symposium on Mixed and Augmented Reality.* IEEE.

Wang, K., T. Shi, G. Liao, and Q. Xia. 2013. "Image registration using a point-line duality based line matching method." *Journal of Visual Communication and Image Representation* 24 (5): 615-626.

Wang, L., U. Neumann, and S. You. 2009. "Wide-baseline image matching using line signatures." *IEEE 12th International Conference on Computer Vision.* 1311-1318.

Wang, Z., F. Wu, and Z. Hu. 2009. "MSLD: A robust descriptor for line matching." *Pattern Recognition*, 941-953.

Wolfson, H. J., and I. Rigoutsos. 1997. "Geometric Hashing: An Overview." *IEEE Computer Science and Engineering* (IEEE) 4 (4): 10-21.

Xiang, Y., C. Song, R. Mottaghi, and S. Savarese. 2014. "Monocular Multiview Object Tracking with 3D Aspect Parts." *European Conference on Computer Vision (ECCV).*

Yamaguchi, M., H. Saito, and S. Yachida. 2017. "Application of LSD-SLAM for Visualzation Temperature in Wide-area Environment." *International Conference on Computer Vision Theory and Applications.* 325-332.

Yang, Liming. 2016. "Point Pattern Matching for Augmented Reality." PhD Thesis.

Zhang. 2000. "A flexible new technique for camera calibration." *IEEE Transactions on Pattern Analysis and Machine Intelligence* 22: 1330–1334.

Zhang, L., and R. Koch. 2013. "An efficient and robust line segment matching approach based on LBD descriptor and pairwise geometric consistency." Edited by Elsevier. *Journal of Visual Communication and Image Representation* 24(7): 794-805.

Zhang, Z. 2000. "A flexible new technique for camera calibration." *IEEE Transactions on Pattern Analysis and Machine Intelligence* 22: 1330–1334.